PHYSICAL REVIEW C **72**, 014904 (2005)

Azimuthal anisotropy in Au+Au collisions at $\sqrt{s_{NN}} = 200$ GeV

J. Adams,[3] M. M. Aggarwal,[29] Z. Ahammed,[43] J. Amonett,[20] B. D. Anderson,[20] D. Arkhipkin,[13] G. S. Averichev,[12] S. K. Badyal,[19] Y. Bai,[27] J. Balewski,[17] O. Barannikova,[32] L. S. Barnby,[3] J. Baudot,[18] S. Bekele,[28] V. V. Belaga,[12] R. Bellwied,[46] J. Berger,[14] B. I. Bezverkhny,[48] S. Bharadwaj,[33] A. Bhasin,[19] A. K. Bhati,[29] V. S. Bhatia,[29] H. Bichsel,[45] J. Bielcik,[48] J. Bielcikova,[48] A. Billmeier,[46] L. C. Bland,[4] C. O. Blyth,[3] B. E. Bonner,[34] M. Botje,[27] A. Boucham,[38] A. V. Brandin,[25] A. Bravar,[4] M. Bystersky,[11] R. V. Cadman,[1] X. Z. Cai,[37] H. Caines,[48] M. Calderón de la Barca Sánchez,[17] J. Castillo,[21] O. Catu,[48] D. Cebra,[7] Z. Chajecki,[44] P. Chaloupka,[11] S. Chattopadhyay,[43] H. F. Chen,[36] Y. Chen,[8] J. Cheng,[41] M. Cherney,[10] A. Chikanian,[48] W. Christie,[4] J. P. Coffin,[18] T. M. Cormier,[46] J. G. Cramer,[45] H. J. Crawford,[6] D. Das,[43] S. Das,[43] M. M. de Moura,[35] A. A. Derevschikov,[31] L. Didenko,[4] T. Dietel,[14] S. M. Dogra,[19] W. J. Dong,[8] X. Dong,[36] J. E. Draper,[7] F. Du,[48] A. K. Dubey,[15] V. B. Dunin,[12] J. C. Dunlop,[4] M. R. Dutta Mazumdar,[43] V. Eckardt,[23] W. R. Edwards,[21] L. G. Efimov,[12] V. Emelianov,[25] J. Engelage,[6] G. Eppley,[34] B. Erazmus,[38] M. Estienne,[38] P. Fachini,[4] J. Faivre,[18] R. Fatemi,[17] J. Fedorisin,[12] K. Filimonov,[21] P. Filip,[11] E. Finch,[48] V. Fine,[4] Y. Fisyak,[4] K. Fomenko,[12] J. Fu,[41] C. A. Gagliardi,[39] L. Gaillard,[3] J. Gans,[48] M. S. Ganti,[43] L. Gaudichet,[38] F. Guerts,[34] V. Ghazikhanian,[8] P. Ghosh,[43] J. E. Gonzalez,[8] O. Grachov,[46] O. Grebenyuk,[27] D. Grosnick,[42] S. M. Guertin,[8] Y. Guo,[46] A. Gupta,[19] T. D. Gutierrez,[7] T. J. Hallman,[4] A. Hamed,[46] D. Hardtke,[21] J. W. Harris,[48] M. Heinz,[2] T. W. Henry,[39] S. Hepplemann,[30] B. Hippolyte,[18] A. Hirsch,[32] E. Hjort,[21] G. W. Hoffmann,[40] H. Z. Huang,[8] S. L. Huang,[36] E. W. Hughes,[5] T. J. Humanic,[28] G. Igo,[8] A. Ishihara,[40] P. Jacobs,[21] W. W. Jacobs,[17] M. Janik,[44] H. Jiang,[8] P. G. Jones,[3] E. G. Judd,[6] S. Kabana,[2] K. Kang,[41] M. Kaplan,[9] D. Keane,[20] V. Yu. Khodyrev,[31] J. Kiryluk,[22] A. Kisiel,[44] E. M. Kislov,[12] J. Klay,[21] S. R. Klein,[21] D. D. Koetke,[42] T. Kollegger,[14] M. Kopytine,[20] L. Kotchenda,[25] M. Kramer,[26] P. Kravtsov,[25] V. I. Kravtsov,[31] K. Krueger,[1] C. Kuhn,[18] A. I. Kulikov,[12] A. Kumar,[29] R. Kh. Kutuev,[13] A. A. Kuznetsov,[12] M. A. C. Lamont,[48] J. M. Landgraf,[4] S. Lange,[14] F. Laue,[4] J. Lauret,[4] A. Lebedev,[4] R. Lednicky,[12] S. Lehocka,[12] M. J. LeVine,[4] C. Li,[36] Q. Li,[46] Y. Li,[41] G. Lin,[48] S. J. Lindenbaum,[26] M. A. Lisa,[28] F. Liu,[47] L. Liu,[47] Q. J. Liu,[45] Z. Liu,[47] T. Ljubicic,[4] W. J. Llope,[34] H. Long,[8] R. S. Langacre,[4] M. Lopez-Noriega,[28] W. A. Love,[4] Y. Lu,[47] T. Ludlam,[4] D. Lynn,[4] G. L. Ma,[37] J. G. Ma,[8] Y. G. Ma,[37] D. Magestro,[28] S. Mahajan,[19] D. P. Mahapatra,[15] R. Majka,[48] L. K. Mangotra,[19] R. Manweiler,[42] S. Margetis,[20] C. Markert,[20] L. Martin,[38] J. N. Marx,[21] H. S. Matis,[21] Yu. A. Matulenko,[31] C. J. McClain,[1] T. S. McShane,[10] F. Meissner,[21] Yu. Melnick,[31] A. Meschanin,[31] M. L. Miller,[22] N. G. Minaev,[31] C. Mironov,[20] A. Mischke,[27] D. K. Mishra,[15] J. Mitchell,[34] B. Mohanty,[43] L. Molnar,[32] C. F. Moore,[40] D. A. Morozov,[31] M. G. Munhoz,[35] B. K. Nandi,[43] S. K. Nayak,[19] T. K. Nayak,[43] J. M. Nelson,[3] P. K. Netrakanti,[43] V. A. Nikitin,[13] L. V. Nogach,[31] S. B. Nurushev,[31] G. Odyniec,[21] A. Ogawa,[4] V. Okorokov,[25] M. Oldenburg,[21] D. Olson,[21] S. K. Pal,[43] Y. Panebratsev,[12] S. Y. Panitkin,[4] A. I. Pavlinov,[46] T. Pawlak,[44] T. Peitzmann,[27] V. Perevoztchikov,[4] C. Perkins,[6] W. Peryt,[44] V. A. Petrov,[13] S. C. Phatak,[15] R. Picha,[7] M. Planinic,[49] J. Pluta,[44] N. Porile,[32] J. Porter,[45] A. M. Poskanzer,[21] M. Potekhin,[4] E. Potrebenikova,[12] B. V. K. S. Potukuchi,[19] D. Prindle,[45] C. Pruneau,[46] J. Putschke,[23] G. Rakness,[30] R. Raniwala,[33] S. Raniwala,[33] O. Ravel,[38] R. L. Ray,[40] S. V. Razin,[12] D. Reichhold,[32] J. G. Reid,[45] G. Renault,[38] F. Retiere,[21] A. Ridiger,[25] H. G. Ritter,[21] J. B. Roberts,[34] O. V. Rogachevskiy,[12] J. L. Romero,[7] A. Rose,[46] C. Roy,[38] L. Ruan,[36] R. Sahoo,[15] I. Sakrejda,[21] S. Salur,[48] J. Sandweiss,[48] M. Sarsour,[17] I. Savin,[13] P. S. Sazhin,[12] J. Schambach,[40] R. P. Scharenberg,[32] N. Schmitz,[23] K. Schweda,[21] J. Seger,[10] P. Seyboth,[23] E. Shahaliev,[12] M. Shao,[36] W. Shao,[5] M. Sharma,[29] W. Q. Shen,[37] K. E. Shestermanov,[31] S. S. Shimanskiy,[12] E. Sichtermann,[21] F. Simon,[23] R. N. Singaraju,[43] G. Skoro,[12] N. Smirnov,[48] R. Snellings,[27] G. Sood,[42] P. Sorensen,[21] J. Sowinski,[17] J. Speltz,[18] H. M. Spinka,[1] B. Srivastava,[32] A. Stadnik,[12] T. D. S. Stanislaus,[42] R. Stock,[14] A. Stolpovsky,[46] M. Strikhanov,[25] B. Stringfellow,[32] A. A. P. Suaide,[35] E. Sugarbaker,[28] C. Suire,[4] M. Sumbera,[11] B. Surrow,[22] T. J. M. Symons,[21] A. Szanto de Toledo,[35] P. Szarwas,[44] A. Tai,[8] J. Takahashi,[35] A. H. Tang,[27] T. Tarnowsky,[32] D. Thein,[8] J. H. Thomas,[21] S. Timoshenko,[25] M. Tokarev,[12] T. A. Trainor,[45] S. Trentalange,[8] R. E. Tribble,[39] O. D. Tsai,[8] J. Ulery,[32] T. Ullrich,[4] D. G. Underwood,[1] A. Urkinbaev,[12] G. Van Buren,[4] M. van Leeuwen,[21] A. M. Vander Molen,[24] R. Varma,[16] I. M. Vasilevski,[13] A. N. Vasiliev,[31] R. Vernet,[18] S. E. Vigdor,[17] Y. P. Viyogi,[43] S. Vokal,[12] S. A. Voloshin,[46] M. Vznuzdaev,[25] W. T. Waggoner,[10] F. Wang,[32] G. Wang,[20] G. Wang,[5] X. L. Wang,[36] Y. Wang,[40] Y. Wang,[41] Z. M. Wang,[36] H. Ward,[40] J. W. Watson,[20] J. C. Webb,[17] R. Wells,[28] G. D. Westfall,[24] A. Wetzler,[21] C. Whitten Jr.,[8] H. Wieman,[21] S. W. Wissink,[17] R. Witt,[2] J. Wood,[8] J. Wu,[36] N. Xu,[21] Z. Xu,[4] Z. Z. Xu,[36] E. Yamamoto,[21] P. Yepes,[34] V. I. Yurevich,[12] Y. V. Zanevsky,[12] H. Zhang,[4] W. M. Zhang,[20] Z. P. Zhang,[36] R. Zoulkarneev,[13] Y. Zoulkarneeva,[13] and A. N. Zubarev[12]

(STAR Collaboration)

[1]*Argonne National Laboratory, Argonne, Illinois 60439, USA*
[2]*University of Bern, CH-3012 Bern, Switzerland*
[3]*University of Birmingham, Birmingham, United Kingdom*
[4]*Brookhaven National Laboratory, Upton, New York 11973, USA*
[5]*California Institute of Technology, Pasadena, California 91125, USA*
[6]*University of California, Berkeley, California 94720, USA*
[7]*University of California, Davis, California 95616, USA*
[8]*University of California, Los Angeles, California 90095, USA*
[9]*Carnegie Mellon University, Pittsburgh, Pennsylvania 15213, USA*

[10]*Creighton University, Omaha, Nebraska 68178, USA*
[11]*Nuclear Physics Institute AS CR, 250 68 Řež/Prague, Czech Republic*
[12]*Laboratory for High Energy (JINR), Dubna, Russia*
[13]*Particle Physics Laboratory (JINR), Dubna, Russia*
[14]*University of Frankfurt, Frankfurt, Germany*
[15]*Institute of Physics, Bhubaneswar 751005, India*
[16]*Indian Institute of Technology, Mumbai, India*
[17]*Indiana University, Bloomington, Indiana 47408, USA*
[18]*Institut de Recherches Subatomiques, Strasbourg, France*
[19]*University of Jammu, Jammu 180001, India*
[20]*Kent State University, Kent, Ohio 44242, USA*
[21]*Lawrence Berkeley National Laboratory, Berkeley, California 94720, USA*
[22]*Massachusetts Institute of Technology, Cambridge, Massachusetts 02139, USA*
[23]*Max-Planck-Institut für Physik, Munich, Germany*
[24]*Michigan State University, East Lansing, Michigan 48824, USA*
[25]*Moscow Engineering Physics Institute, Moscow, Russia*
[26]*City College of New York, New York City, New York 10031, USA*
[27]*NIKHEF, Amsterdam, The Netherlands*
[28]*Ohio State University, Columbus, Ohio 43210, USA*
[29]*Panjab University, Chandigarh 160014, India*
[30]*Pennsylvania State University, University Park, Pennsylvania 16802, USA*
[31]*Institute of High Energy Physics, Protvino, Russia*
[32]*Purdue University, West Lafayette, Indiana 47907, USA*
[33]*University of Rajasthan, Jaipur 302004, India*
[34]*Rice University, Houston, Texas 77251, USA*
[35]*Universidade de Sao Paulo, Sao Paulo, Brazil*
[36]*University of Science & Technology of China, Anhui 230027, China*
[37]*Shanghai Institute of Applied Physics, Shanghai 201800, China*
[38]*SUBATECH, Nantes, France*
[39]*Texas A&M University, College Station, Texas 77843, USA*
[40]*University of Texas, Austin, Texas 78712, USA*
[41]*Tsinghua University, Beijing 100084, China*
[42]*Valparaiso University, Valparaiso, Indiana 46383, USA*
[43]*Variable Energy Cyclotron Centre, Kolkata 700064, India*
[44]*Warsaw University of Technology, Warsaw, Poland*
[45]*University of Washington, Seattle, Washington 98195, USA*
[46]*Wayne State University, Detroit, Michigan 48201, USA*
[47]*Institute of Particle Physics, CCNU (HZNU), Wuhan 430079, China*
[48]*Yale University, New Haven, Connecticut 06520, USA*
[49]*University of Zagreb, Zagreb, HR-10002, Croatia*

A. Braem,[1] M. Davenport,[1] G. De Cataldo,[2] D. Di Bari,[2] P. Martinengo,[1] E. Nappi,[2] G. Paic,[3] E. Posa,[2] F. Puiz,[1] and E. Schyns[1]
(STAR-RICH Collaboration)
[1]*CERN, Switzerland*
[2]*INFN, Sez. Di Bari, Bari, Italy*
[3]*Instituto de Ciencias Nucleares, UNAM, Mexico*

(Received 29 September 2004; revised manuscript received 3 February 2005; published 14 July 2005)

The results from the STAR Collaboration on directed flow (v_1), elliptic flow (v_2), and the fourth harmonic (v_4) in the anisotropic azimuthal distribution of particles from Au+Au collisions at $\sqrt{s_{NN}} = 200$ GeV are summarized and compared with results from other experiments and theoretical models. Results for identified particles are presented and fit with a blast-wave model. Different anisotropic flow analysis methods are compared and nonflow effects are extracted from the data. For v_2, scaling with the number of constituent quarks and parton coalescence are discussed. For v_4, scaling with v_2^2 and quark coalescence are discussed.

DOI: 10.1103/PhysRevC.72.014904 PACS number(s): 25.75.Ld

I. INTRODUCTION

In heavy-ion collisions at the Relativistic Heavy Ion Collider (RHIC), the initial spatially anisotropic participant zone evolves, via possible novel phases of nuclear matter, into the observed final state, consisting of large numbers of produced particles with anisotropic momentum distributions in the transverse plane. Important insights into the evolution may be obtained from the study of this azimuthal anisotropy, most of which is believed to originate at the early stages of the collision process. Unlike at lower beam energies [1], the measured anisotropies at RHIC reach the large values predicted by hydrodynamic models and conform to the particle mass dependence expected from hydrodynamics in the kinematic region where this type of model is expected to be applicable (i.e., for transverse momenta below a couple of GeV/c [2]. The large observed anisotropy at RHIC is argued to be indicative of early local thermal equilibrium, and the particle mass dependence is highly relevant to interpretations involving a strongly interacting quark gluon plasma phase [2–4]. At larger transverse momenta, measurements of azimuthal anisotropy are also relevant to the observation of jet quenching [5,6]. Given the current debate around these interpretations, we summarize STAR's findings to date in the area of azimuthal anisotropy, present additional results for identified particles, compare in detail the different analysis methods and their systematic uncertainties, compare the data to various models, and systematize the results with fits to the hydrodynamic motivated blast wave model.

The article is organized into sections on the experiment, methods of analysis, results, comparison of analysis methods, comparison of results to various models, and conclusions. The methods comparisons section is rather technical, dealing with systematic errors, nonflow effects, and fluctuations.

II. EXPERIMENT

The main detectors of the STAR experiment used in these analyses are the time projection chamber (TPC) [7] and the forward TPCs (FTPCs) [8]. The ring imaging Cherenkov detector (RICH) [9] of the STAR-RICH collaboration is also used for particle identification. The cuts on the data for most of the TPC analyses are described in Table I, except for the upper p_t cutoff, which often goes higher as shown in the graphs. For the FTPCs the pseudorapidity acceptance is $2.4 < |\eta| < 4.2$, only at least five hits are required, the distance of closest approach of the track to the vertex (dca) is restricted to less than 3 cm, and for the v_1 analysis the vertex z is opened up to ± 50 cm. The RICH detector [9] covers $|\eta| < 0.30$ with a 20° bite in azimuth. The RICH detector separates charged mesons from protons+antiprotons identified track by track. The admixture of baryons in the meson sample is always less than 10%. The momenta of the particles identified in the RICH come from tracking in the TPC.

The data were collected with a minimum bias trigger that required a coincidence from the two zero-degree calorimeters, with each signal being greater than 1/4 of the single neutron peak and arriving within a time window centered for the interaction diamond. The centrality definition, which is based on the raw charged particle TPC multiplicity with $|\eta| < 0.5$, is the same as used previously [10]. The centrality bins are specified in Table II. The mean charged particle multiplicity given in Table II is for the cuts in Table I. The estimated values in the table come from a Monte Carlo Glauber (MCG) model calculation [11]. In this calculation, the number of participants is equal to the number of wounded nucleons. The estimated errors shown for the calculated quantities come from a linear combination of the changes in the quantities caused by reasonable variations in the parameters of the model. Minimum bias refers to 0 to 80% most central hadronic cross section. Two million events are analyzed for this article. For the analysis involving FTPCs only 70,000 events are available. Errors presented for the data are statistical. Systematic errors are mainly because of the method of analysis, nonflow effects, and fluctuations; these are discussed in Sec. V.

TABLE I. Cuts used in the TPC analysis of Au+Au collisions at $\sqrt{s_{NN}} = 200$ GeV.

Cut	Value
p_t	0.15 to 2.0 GeV/c
η	-1.3 to 1.3
Multiplicity	>10
Vertex z	-25.0 to 25.0 cm
Vertex x, y	-1.0 to 1.0 cm
Fit points	>15
Fit pts/max. pts	>0.52
dca	<2.0 cm
Trigger	Min. bias

Note: Vertex refers to the event vertex, fit points are the space points on a track, and dca is the distance of closest approach of the track to the event vertex.

Several methods are used to identify particles. The energy loss in the gas of the TPC identifies particles at low p_t. For this the probability PID method [12,13] is used, requiring 95% particle purity unless otherwise stated. In the FTPCs the energy loss is not sufficient for good particle identification. The RICH detector can separate mesons from baryons up to higher p_t. Using the characteristic kink decay of K^0_S, one is able to go to higher p_t. Strange particles up to high p_t are identified by their topological decay.

For the kink analysis of charged kaons, flow parameters were measured for particles that decay in flight within a fiducial volume in the TPC. The one-prong decay vertex ("kink") provides topological identification of the particle species with good rejection of background [14]. The main sources of possible misidentification are pion decays, random combinatoric background, and secondary hadronic interactions in the TPC gas. The level of background in the analyzed sample was estimated to be 5–10% but is p_t dependent. Several cuts were applied to the raw signal to remove most of the background. Pion decays were removed by applying a momentum-dependent decay angle cut, which exploits differences in the decay kinematics. Other cuts were also applied to the dE/dx, pseudorapidity, and invariant mass of

TABLE II. Listed for $\sqrt{s_{NN}} = 200\,\text{GeV}$ for each centrality bin are the range of the percentage most central of the hadronic cross section and its mean value, the mean charged particle multiplicity with its standard deviation spread, the estimated mean number of wounded nucleons, the estimated mean number of binary collisions, and the estimated mean impact parameter, with the uncertainties in these quantities.

Centrality bin	1	2	3	4	5	6	7	8	9
Percentage most central	70–80	60–70	50–60	40–50	30–40	20 –30	10–20	5–10	0–5
$\langle centrality \rangle$ (%)	73.8	64.1	53.9	44.7	35.2	25.4	15.1	7.7	2.3
$\langle M \rangle \pm \sigma$	38 ± 11	76 ± 17	134 ± 24	214 ± 32	323 ± 42	468 ± 53	651 ± 64	819 ± 48	961 ± 56
$\langle N_{\text{WN}} \rangle \pm \sigma$	13 ± 4	26 ± 7	46 ± 9	75 ± 11	114 ± 12	165 ± 12	232 ± 10	298 ± 10	352 ± 6
$\langle N_{\text{binary}} \rangle \pm \sigma$	11 ± 5	28 ± 10	61 ± 17	120 ± 28	216 ± 38	364 ± 51	587 ± 61	825 ± 72	1049 ± 72
$\langle b \rangle \pm \sigma$ (fm)	13.2 ± 0.6	12.3 ± 0.6	11.3 ± 0.6	10.2 ± 0.5	9.0 ± 0.5	7.6 ± 0.4	5.9 ± 0.3	4.2 ± 0.3	2.3 ± 0.2

the parent track candidate, to the daughter momentum, and to the distance of closest approach associated with the two track segments at the kink vertex. Finally, there was a quality cut to remove candidates with vertices inside the TPC sector gaps where spurious kink vertices can arise [14]. Currently the kink method can reconstruct charged kaons up to $p_t \sim 4\,\text{GeV}/c$. The tracking software has difficulty resolving a kink vertex when the decay angle is less than about 6°. For kaons with $p_t > 3\,\text{GeV}/c$, the decay angle is almost always around 6° or less, so efficiency falls off rapidly above 3 GeV/c. The efficiency also suffers from the limited fiducial volume; the kaon must decay inside a small subvolume of the TPC to provide adequate track length for both parent and daughter tracks.

Other strange particles were identified by their decay topology [15,16]. These methods used for the strange particle decays have already been described [15,17].

III. METHODS OF ANALYSIS

Directed and elliptic flow are defined as the first, v_1, and second, v_2, harmonics in the Fourier expansion of the particle azimuthal anisotropic distribution with respect to the reaction plane. The reaction plane contains the collision impact parameter. However, normally measurements are made relative to the observed event plane and are corrected for the resolution of the event plane relative to the reaction plane. The event plane angle is defined for each harmonic, n, by the angle, Ψ_n, of the flow vector, Q, whose x and y components are given by the following:

$$\begin{aligned} Q_n \cos(n\Psi_n) &= \sum [w_i \cos(n\phi_i)] \\ Q_n \sin(n\Psi_n) &= \sum [w_i \sin(n\phi_i)], \end{aligned} \tag{1}$$

where the ϕ_i are the azimuthal angles of all the particles used to define the event plane and the weights, w_i, are used to optimize the event plane resolution. In this article the weights for the even harmonics have been taken to be proportional to p_t up to 2 GeV/c and constant above that. For the odd harmonics they have been taken to be proportional to η for $|\eta| > 1$.

STAR has previously presented results using different methods of analysis. In the standard method [18], denoted by v_n, particles are correlated with an event plane of the same harmonic. Using this method STAR has presented results on elliptic flow (v_2) for charged hadrons [5,19], identified particles [12], strange particles [15,20], and multistrange baryons [17]. In the N-particle cumulant method [21], denoted by $v_n\{N\}$, N-particle correlations are calculated and nonflow effects subtracted to first order when N is greater than 2. Nonflow effects that affect v_n are particle correlations that are not correlated with the reaction plane. Two-particle cumulants should give essentially the same results and errors as the standard method, but multiparticle cumulants have larger statistical errors. STAR has presented four-particle cumulant results [22] for charged hadrons. In three-particle mixed harmonic methods relative to the second-harmonic event plane, denoted by $v_n\{\text{EP}_2\}$ when $n \neq 2$, the particles of a different harmonic are correlated with the well-determined second harmonic event plane. With mixed harmonics, nonflow effects are greatly suppressed. With this method STAR has reported results on directed flow (v_1) [23–25] and higher harmonics (v_4) [23,26] for charged hadrons.

A. Directed flow methods

Because directed flow goes to zero at midrapidity by symmetry, the first-harmonic event plane is poorly defined in the TPC. A better way to measure v_1 is to use mixed harmonics involving the second-harmonic event plane; this also suppresses nonflow contributions at the same time. One such method is the three particle cumulant method that has been described [27].

We also measure v_1 using another mixed-harmonic technique: we determine two first-order reaction planes $\Psi_1^{\text{FTPC}_1}$ and $\Psi_1^{\text{FTPC}_2}$ in the FTPCs and the second-order reaction plane Ψ_2^{TPC} in the TPC. Using the recently proposed notation (see Ref. [23]) we denote this measurement as $v_1\{\text{EP}_1, \text{EP}_2\}$.

$$v_1\{\text{EP}_1, \text{EP}_2\} = \frac{\left\langle \cos\left(\phi + \Psi_1^{\text{FTPC}} - 2\Psi_2^{\text{TPC}}\right)\right\rangle}{\sqrt{\left\langle \cos\left(\Psi_1^{\text{FTPC}_1} + \Psi_1^{\text{FTPC}_2} - 2\Psi_2^{\text{TPC}}\right)\right\rangle \times \text{Res}\left(\Psi_2^{\text{TPC}}\right)}}, \tag{2}$$

where the ϕ of the particle is correlated with the Ψ_1^{FTPC} in the other subevent and

$$\text{Res}\left(\Psi_2^{\text{TPC}}\right) = \langle \cos[2(\Psi_2 - \Psi_{\text{RP}})] \rangle \tag{3}$$

represents the resolution of the second-order event plane measured in the TPC. This resolution, as usual, is derived from

the square root of the correlation of TPC subevent planes. For the derivation of Eq. (2) see Appendix B.

This new v_1 method also provides an elegant tool to determine the sign of v_2. One of the quantities involved in the above measurement of $v_1\{\mathrm{EP}_1, \mathrm{EP}_2\}$ [see Appendix B, Eq. (B3) and compare to Ref. [18], Eq. (18)] is approximately proportional to the product of integrated values of v_1^2 and v_2. Applying factors for weights and multiplicities [18] leads to the following:

$$v_1^2 \times v_2 \approx \left(\frac{4}{\pi}\right)^{\frac{3}{2}} \sqrt{\prod_d \frac{1}{M_d} \frac{\langle w_d^2 \rangle}{\langle w_d \rangle^2}} \times \left\langle \cos\left(\Psi_1^{\mathrm{FTPC}_1} + \Psi_1^{\mathrm{FTPC}_2} - 2\Psi_2^{\mathrm{TPC}}\right)\right\rangle, \quad (4)$$

where the index d represents the three detectors used in the analysis: FTPC_1, FTPC_2, and TPC. For each centrality class M_d denotes the corresponding multiplicities and w_d are the applied weights (η weighting for Ψ_1 and p_t weighting for Ψ_2).

B. Elliptic flow methods

The standard method [18] correlates each particle with the event plane determined from the full event minus the particle of interest. Because the event plane is only an approximation to the true reaction plane, one has to correct for this smearing by dividing the observed correlation by the event-plane resolution, which is the correlation of the event plane with the reaction plane. The event-plane resolution is always less than 1, and thus dividing by it raises the flow values. To make this correction the full-event is divided up into two subevents (a and b), and the square root of the correlation of the subevent planes is the subevent-plane resolution. The full-event plane resolution is then obtained using the equations in Ref. [18] that describe the variation of the resolution with multiplicity.

The scalar product method [22] is a simpler variation of this method, which weights events with the magnitude of the flow vector Q as follows:

$$v_n(\eta, p_t) = \frac{\langle Q_n u_{n,i}^*(\eta, p_t)\rangle}{2\sqrt{\langle Q_n^a Q_n^{b*}\rangle}}, \quad (5)$$

where $u_{n,i} = \cos(n\phi_i) + i\sin(n\phi_i)$ is the unit vector of the ith particle. If Q_n is replaced by its unit vector, the above reduces to the standard method. Taking into account the nonflow contribution, the numerator of Eq. (5) can be written as follows [6,22]:

$$\left\langle \sum_i \cos 2(\phi_{p_t} - \phi_i) \right\rangle = M v_2(p_t)\, \bar{v}_2 + \{\text{nonflow}\} \quad (6)$$

where ϕ_{p_t} is the azimuthal angle of the particle from a given p_t bin. The first term in the right-hand side of Eq. (6) represents the elliptic flow contribution, where $v_2(p_t)$ is the elliptic flow of particles with a given p_t, $\bar{v}_2$ is the average flow of particles used in the sum, and M is the multiplicity of particles contributing to the sum, which in this article is performed over particles in the region $0.15 < p_t < 2.0\,\mathrm{GeV}/c$ and $|\eta| < 1.0$.

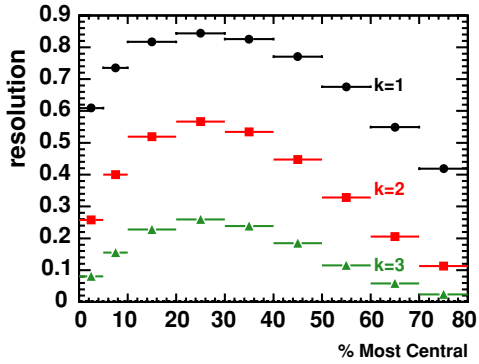

FIG. 1. (Color online) The event plane resolutions as a function of centrality for $v_{k2}\{\mathrm{EP}_2\}$.

The cumulant method has been well described [21,28] and previously used for the analysis of STAR data [22].

To reduce the nonflow effects from intrajet correlations at high transverse momentum, we also use a modified event-plane reconstruction algorithm, where all subevent particles in a pseudorapidity region of $|\Delta\eta| < 0.5$ around the highest p_t particle in the event are excluded from the event-plane determination. With this modified event plane method, the full-event-plane resolution is 15–20% worse than with the standard method because of the smaller number of tracks used for the event plane determination.

C. Higher harmonic methods

Because the second-harmonic event plane is determined so well, one can try to determine the higher even harmonics of the azimuthal anisotropy by correlating particles with the second-harmonic event plane. However, then the event-plane resolution is worse because of the various possible orientations of the higher harmonics relative to the second-harmonic event plane. Taking k to be the ratio of the higher harmonic number to the event-plane harmonic number and using the equations in Ref. [18] we obtain the resolutions in Fig. 1 for $v_{k2}\{\mathrm{EP}_2\}$. This method works when the resolution of the standard method ($k = 1$) is large and therefore those for the higher harmonics are not too low. Also, these $k \neq 1$ methods use mixed harmonics, which involve multiparticle correlations, greatly reducing the nonflow contributions.

The cumulant method with mixed harmonics has also been used for v_4 [23].

IV. RESULTS

In the following sections we present results for directed flow, elliptic flow, and the higher harmonics. Some of the graphs have model calculations on them that are discussed in Sec. VI. The tables of data for this article are available at http://www.star.bnl.gov/central/publications/.

A. Directed flow, $v_1\{\mathrm{EP}_1, \mathrm{EP}_2\}$

The STAR TPC has very good capabilities to measure elliptic flow at midrapidity, whereas the FTPCs allow one to measure directed flow. Figure 2 plots directed flow as a function of pseudorapidity, showing that v_1 appears to

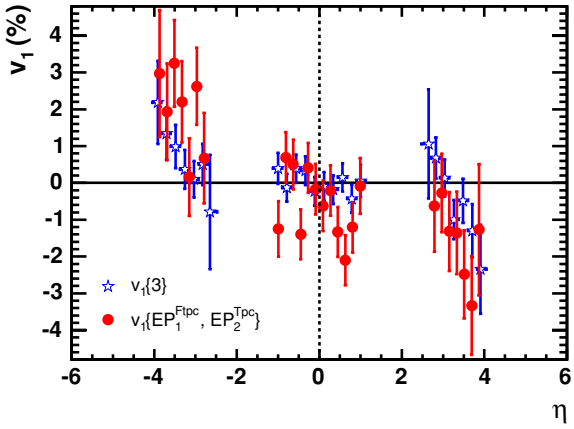

FIG. 2. (Color online) Directed flow of charged hadrons as a function of pseudorapidity. The measurements of $v_1\{\mathrm{EP}_1, \mathrm{EP}_2\}$ (circles; centrality 20–60%) agree with the published results of $v_1\{3\}$ (stars; centrality 10–70%).

be close to zero near midrapidity. First, the analysis was done successfully on simulated data containing a fixed v_1. For real data, using random subevents in the two FTPCs to determine $\Psi_1^{\mathrm{FTPC}_1}$ and $\Psi_1^{\mathrm{FTPC}_2}$ in Eq. (2), the results are in agreement with the published measurements obtained by the three-particle cumulant method $v_1\{3\}$ [23,24], as shown in Fig. 2. Recently, PHOBOS has also reported [29] v_1 values using a two-particle correlation method. Although we approximately agree at $\eta = 4.0$, they have finite values at $\eta = 2.5$–3.0, whereas ours are close to zero, as can be seen for ours in Fig. 2.

The sign of v_2 determines whether the elliptic flow is in plane or out of plane. Although the sign of v_2 had been determined to be positive from three particle correlations [23], the above new method for v_1 allows another method based on the sign of $v_1^2 v_2$. Because v_1^2 is always positive, the sign of $v_1^2 v_2$ determines the sign of v_2.

Averaged over centralities 20–60% we measure $v_1^2 \times v_2$ in Fig. 3 to be $(2.38 \pm 0.99) \times 10^{-5}$. This is only a 2.4 sigma effect and if 10% systematic errors are assumed based on Sec. V for both v_1 and v_2 this becomes a 2.2 sigma effect. Only

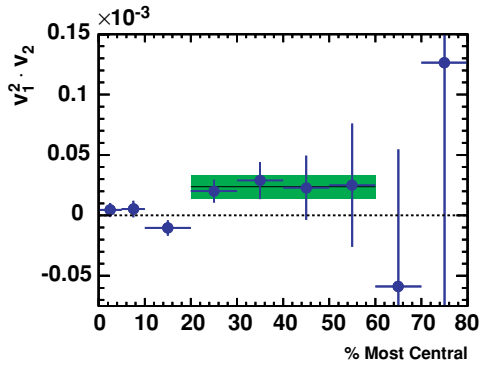

FIG. 3. (Color online) The product of v_1^2 and v_2. The shaded band is the mean value of this quantity with its error, averaged over centralities 20–60%. Because this quantity is positive, elliptic flow is measured to be *in plane*.

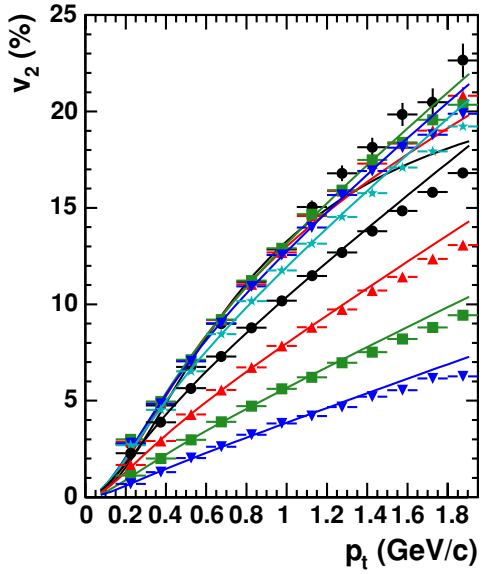

FIG. 4. (Color online) Charged hadron v_2 vs. p_t for the centrality bins (bottom to top) 5 to 10% and in steps of 10% starting at 10, 20, 30, 40, 50, 60, and 70 up to 80%. The solid lines are blast-wave fits.

the midcentrality bins are averaged because in this centrality region the expected nonflow contributions are much smaller than for the more central and peripheral bins. Therefore, with these caveats, the sign of v_2 is confirmed to be positive: *in-plane* elliptic flow.

B. Elliptic flow, v_2

There have been many elliptic flow results from RHIC. STAR has extensive systematics that we present and compare to the other experiments. Many of the graphs contain blast-wave model fits that are discussed under Sec. VI D. We present data separately for the central rapidity region, the forward region, and for high p_t.

1. The central region

The $v_2(p_t)$ values for charged hadrons for individual centralities are shown in Fig. 4 with blast-wave fits performed assuming that all charged hadrons have the mass of the pion. The data are well reproduced by the blast-wave parametrization when p_t is below 1 GeV/c. Above this limit, the contribution of protons in the charged hadron sample becomes significant and changes with centrality, which challenges the pion mass assumption. Furthermore it has been found that hydrodynamic flow may not be applicable above 1 GeV/c, especially for light particles, as new phenomena such as hadronization by recombination may become significant [30].

Although all the data presented in this article were collected using the full magnetic field (0.5 T) of the STAR detector, some data were also collected using half the magnetic field. Below 0.5 GeV/c the half-field v_2 values are lower, especially for the more central collisions. These are regions where the v_2 values are small. Adding the absolute value of 0.0025 to the half-field $v_2(p_t)$ data brought the two sets of data into approximate agreement in this p_t range. This additive value

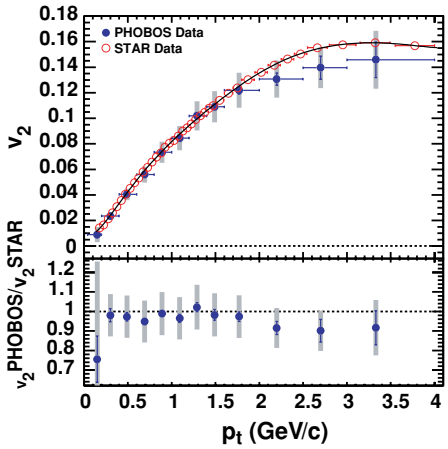

FIG. 5. (Color online) v_2 vs. p_t for charged hadrons from 0–50% centrality collisions in comparison to data from PHOBOS [29]. The line is a polynomial fit to the STAR data. The gray error boxes represent the PHOBOS systematic errors. The bottom panel shows the ratio of the PHOBOS data to the polynomial fit.

is for both sets of data analyzed with a dca cut of 2 cm as is done in this article. The discrepancy gets worse as the upper dca cut decreases. The effect is not understood and none of the half-field data are included in this article. However, a possible explanation is that the half-field data have poorer two-track resolution and are more sensitive to track merging, giving a negative nonflow contribution. If true, there could be a possible small residual systematic effect on the full-field data. However, the v_2 results are compared to PHOBOS data [29] for 0–50% centrality and $0 < \eta < 1.5$ in Fig. 5. The STAR data is for the TPC integrated also for 0–50% centrality. The full-field data presented here agree well with the PHOBOS data.

Results from four-particle cumulants, $v_2\{4\}$, are shown in Fig. 6 for particles identified by energy loss in the TPC. Also shown are hydrodynamic calculations [31]. The two-particle values, $v_2\{2\}$ for pions, kaons, and antiprotons are shown for the individual centralities with blast-wave fits in Fig. 7. We use only antiprotons at low p_t because of contamination of the proton sample from hadronic interactions in the detector material.

Figure 8 shows $v_2(p_t)$ for charged mesons and protons + antiprotons identified in the RICH detector. The experimental results are compared to hydrodynamic calculations [31]. In

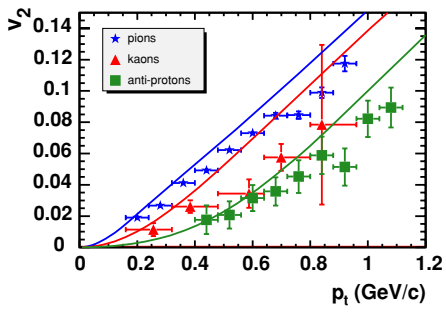

FIG. 6. (Color online) $v_2\{4\}$ vs. p_t for identified particles in the 20–60% centrality range. The solid lines are hydrodynamic calculations [31].

the hydrodynamic picture, the mass ordering of v_2 (the lighter particles have larger v_2 than the heavier particles) is predicted to hold at all transverse momenta. Up to $p_t \sim 2$ GeV/c, v_2 of charged mesons is found to be larger than that of the heavier baryons, in agreement with hydrodynamic predictions. Above $p_t = 2$ GeV/c, the data seem to indicate a reversed trend where the protons + antiprotons might have larger v_2 values than the charged mesons.

From the kink analysis the results are shown in Fig. 9. There were about 0.4 accepted candidate kaons reconstructed per event.

Results are shown in Fig. 10 comparing STAR data for K^0_S and $\Lambda + \overline{\Lambda}$ out to 6 GeV/c with some PHENIX data [32] and with hydro calculations [60]. For kaons, we can now compare $v_2(p_t)$ for neutral kaons, charged kaons from kinks, and charged kaons from energy loss identification. This is shown in Fig. 9, where the agreement is good, but in the insert one can see that the neutral kaons tend to be slightly lower than the charged kaons.

We can also compare our results in more detail at lower p_t with those from PHENIX [32]. Figure 11 shows $v_2(p_t)$ for charged pions and antiprotons from the energy loss analysis requiring 90% purity and kaons from the kink analysis. The PHENIX results are for $|\eta| < 0.35$, for 0–70% centrality, and for protons and antiprotons combined. In the p_t range where the data overlap, the agreement is seen to be good.

It is interesting to see how azimuthal correlations evolve from elementary collisions ($p+p$) through collisions involving cold nuclear matter (d+Au) and then on to hot, heavy-ion collisions (Au+Au). A convenient quantity for such comparisons is the scalar product. In the case of only "nonflow," the scalar product should be the same for all three collision systems regardless of their system size. This assumes independent collisions and that other effects like short range correlations are small. Thus, deviations of the scalar product from elementary $p+p$ collisions result from collective motion and/or effects of medium modification.

Figure 12 shows the scalar product as defined in Eq. (6) as a function of p_t for three different centrality ranges in Au+Au collisions compared to minimum bias $p+p$ collisions [6] and d+Au collisions. For Au+Au collisions, in middle central events we observe a big deviation from $p+p$ collisions that is because of the presence of elliptic flow, whereas in peripheral events, collisions are essentially like elementary $p+p$ collisions. The azimuthal anisotropy goes up to 10 GeV/c but we cannot distinguish whether it is from hydrolike flow or from jet quenching. For p_t beyond 5 GeV/c in central collisions, we again find a similarity between Au+Au collisions and $p+p$ collisions, indicating the dominance of nonflow effects. The scalar product in d+Au collisions is relatively close to that from $p+p$ collisions but there is a finite difference at low p_t. This difference is small if compared to the difference between middle central Au+Au collisions and minimum bias $p+p$ collisions. If we examine the difference by looking in d+Au collisions at different event classes that are defined by the multiplicity from the Au side (Fig. 13), we find that the scalar product in d+Au increases as a function of multiplicity class, which is contradictory to Au+Au collisions, in which the differences rise and fall as

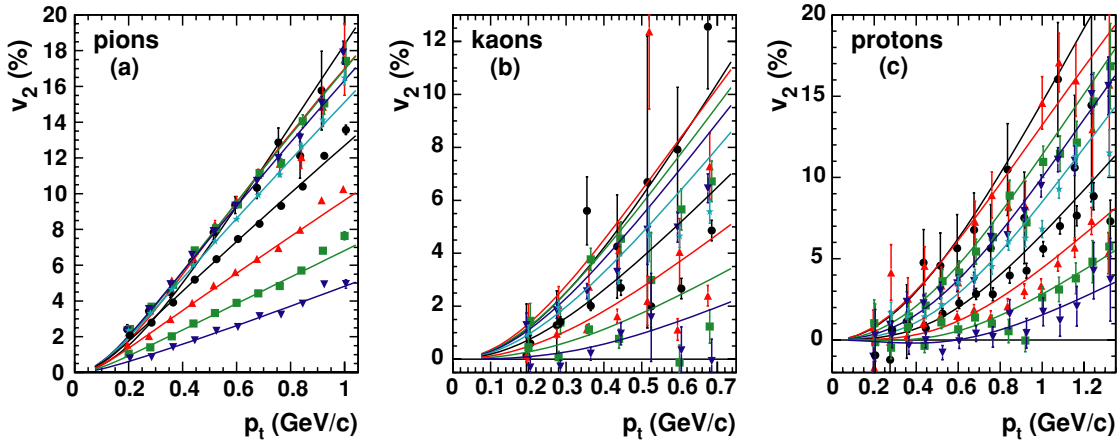

FIG. 7. (Color online) $v_2\{2\}$ vs. p_t for charged pions, charged kaons, and antiprotons for the centrality bins (bottom to top) 5–10% and in steps of 10% starting at 10, 20, 30, 40, 50, 60, and 70 up to 80%. The solid lines are blast-wave fits.

a function of centrality; a typical pattern that is caused by collective flow. The trend in d+Au could be explained by the Cronin effect, because in high-multiplicity events, the Cronin effect is expected to produce more collective motion among soft particles to generate a high-p_t particle [33]. To further test the Cronin effect hypothesis, we studied the asymmetry of the scalar product in d+Au collisions in Fig. 14. The ratio of scalar product from the Au side divided by that from the deuteron side is greater than 1 at low p_t and decreases to ∼0.9 above 2 GeV/c. This indicates that there is more collective motion for $p_t > 2$ GeV/c in the deuteron side and $p_t < 1$ GeV/c in the Au side, which is again consistent with the Cronin effect. Recently, the Cronin effect has been explained by final-state recombination [34]. However the influence of recombination on azimuthal correlations needs detailed study. In addition to spectra, the scalar product results open new possibilities for testing these models.

2. *The forward regions*

Our measurements of elliptic flow $v_2(\eta)$ for charged hadrons at forward pseudorapidities along with those from the central region are shown in Fig. 15. The published results [29,35] obtained by the PHOBOS collaboration showing a bell-shaped curve are confirmed. We observe a falloff by a factor of 1.8 comparing $v_2(\eta = 0)$ with $v_2(\eta = 3)$. Although STAR determined the event plane near midrapidity, PHOBOS did it at forward rapidities, which probably accounts for the slightly less falloff that they see. Both measurements were done using the standard method. Figure 16 compares our results for v_2 obtained with the method of two-particle cumulants, $v_2\{2\}$, to that for four-particle cumulants, $v_2\{4\}$. The difference at midrapidity is discussed in Sec. V. The FTPC $v_2\{4\}$ values are not quite symmetric about midrapidity, but not unreasonable considering the statistical errors. Within the errors in the FTPC regions, the values from the different methods are about the same.

Figure 17 shows $v_2\{4\}(p_t)$ obtained from the four-particle cumulant method. Because there are many more particles in the main TPC than in the FTPCs, these v_2 values are mainly at midrapidity. $v_2\{4\}$, which is much less sensitive to nonflow effects, is compared to $v_2\{2\}$ at forward rapidities, where nonflow may be small. The observed flattening at p_t values around 1 GeV/c for the FTPC measurements might

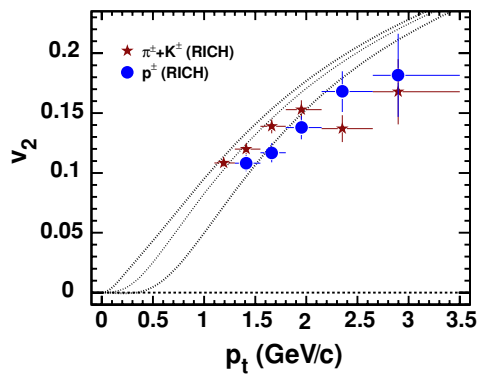

FIG. 8. (Color online) v_2 vs. p_t for particles identified in the RICH detector from minimum bias collisions. The lines are hydrodynamic calculations [31] for pions (upper line), kaons (middle line), and protons (lower line).

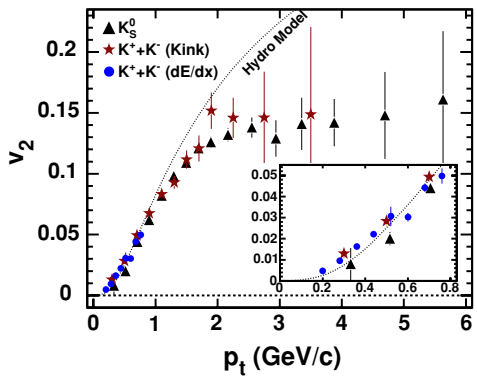

FIG. 9. (Color online) v_2 vs. p_t for neutral and charged kaons for minimum bias collisions. The K^0_S values are from Ref. [20]. The hydrodynamic model line is from Ref. [31]. The insert expands the low p_t region to make the kaons from dE/dx more visible.

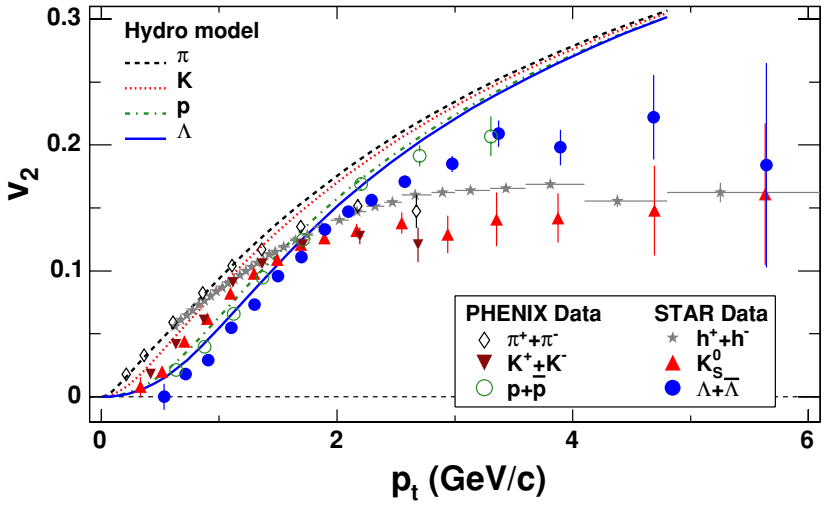

FIG. 10. (Color online) v_2 vs. p_t for strange particles from minimum bias collisions. The STAR K^0_S and $\Lambda + \overline{\Lambda}$ values are from Ref. [20]. The PHENIX data are from Ref. [32]. The hydro calculations are from Ref. [60].

be explained by the momentum resolution of the FTPCs. To quantify the influence of the momentum resolution a Monte Carlo simulation of $v_2(p_t)$ based on the measurements at midrapidity was done, but the input η and p_t spectra were obtained from measurements of the Au+Au minimum bias data at forward rapidities. Results of embedding charged pions (neglecting protons) in real Au+Au events up to 5% of the total multiplicity in the FTPCs were used to estimate the momentum resolution as a function of η and p_t. At $\eta = 3.0$ the momentum resolution goes from 10% at low p_t to 35% at $p_t = 2.0\,\text{GeV}/c$, but gets about a factor of two worse at $\eta = 3.5$. In Fig. 17 the MC simulation $v_2(p_t)$, including the momentum resolution of the FTPCs, seems to explain the observed flattening by smearing low p_t particles to higher p_t. Thus we cannot conclude that the shape of the p_t dependence of elliptic flow at forward rapidities is different from that at midrapidity, even though the values integrated over p_t are considerably smaller as shown in Fig. 16.

3. *High p_t*

Hadron yields at sufficiently high transverse momentum in Au+Au collisions are believed to contain a significant fraction originating from the fragmentation of high-energy partons resulting from initial hard scatterings. Calculations based on perturbative QCD predict that high-energy partons traversing nuclear matter lose energy through induced gluon radiation [36]. Energy loss (jet quenching) is expected to depend strongly on the color charge density of the created system and the traversed path length of the propagating parton. Consistent with jet-quenching calculations, strong suppression of the inclusive high-p_t hadron production [10,37] and back-to-back high-p_t jetlike correlation [38] compared to the reference $p+p$ and $d+$Au systems was measured in central Au+Au collisions at RHIC. In noncentral heavy-ion collisions, the geometrical overlap region has an almond shape in the transverse plane, with its short axis lying in the reaction plane. Partons traversing such a system, on average, experience different path lengths and therefore different energy

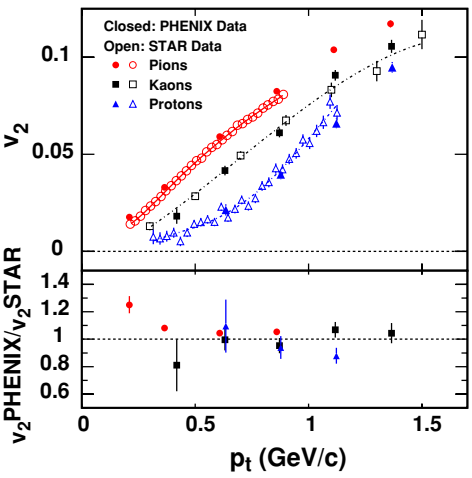

FIG. 11. (Color online) v_2 vs. p_t for charged pions, charged kaons, and antiprotons from minimum bias collisions in comparison to similar data from PHENIX. The lines are polynomial fits to the STAR data. The bottom panel shows the ratio of the PHENIX data to the polynomial fits.

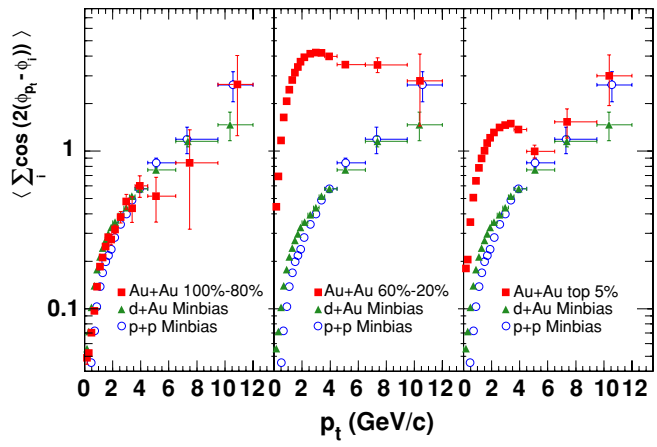

FIG. 12. (Color online) Charged-hadron azimuthal correlations vs. p_t in Au+Au collisions (squares) as a function of centrality (peripheral to central from left to right) compared to minimum bias azimuthal correlations in $p+p$ collisions (circles) and $d+$Au collisions (triangles). The Au+Au and $p+p$ data are from Ref. [6].

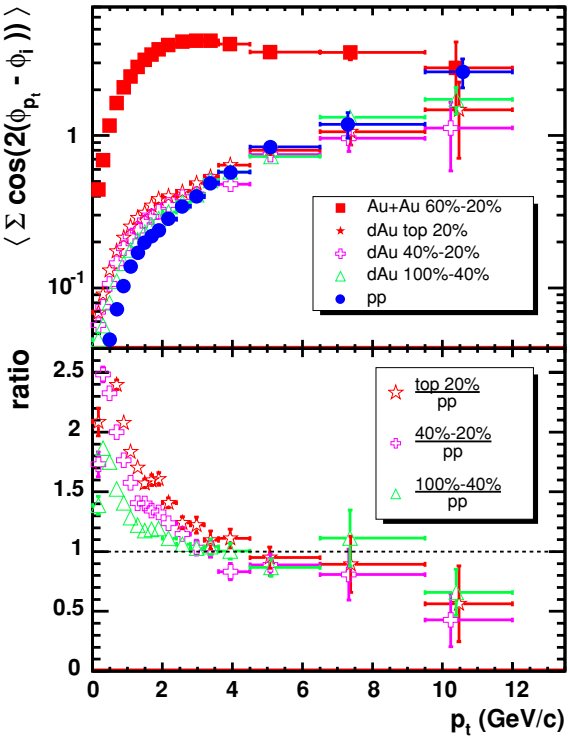

FIG. 13. (Color online) The top panel shows the charged hadron scalar product vs. p_t for different centrality classes in d+Au collisions, and minimum bias p+p collisions. The Au+Au result is put there for a reference. The bottom panel shows the ratio of scalar product from d+Au collisions to minimum bias p+p collisions for three different centrality classes.

loss as a function of their azimuthal angle with respect to the reaction plane. This leads to an azimuthal anisotropy in particle production at high transverse momenta. Finite values of v_2 were measured in noncentral Au+Au collisions for p_t up to ~7–8 GeV/c [5,6] using the standard reaction plane method and two- and four-particle cumulants. The measurements of azimuthal anisotropies at high transverse momenta with the standard reaction plane method and two-particle cumulants are influenced by the contribution from the inter- and intrajet correlations. These correlations, in general, may not be related

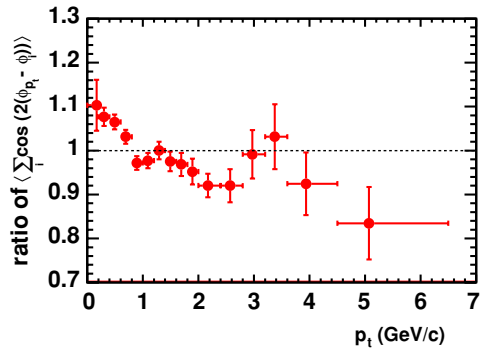

FIG. 14. (Color online) The ratio of the scalar product from the Au side ($-1.0 < \eta < -0.5$) to that from deuteron side ($0.5 < \eta < 1.0$) vs. p_t from minimum bias collisions.

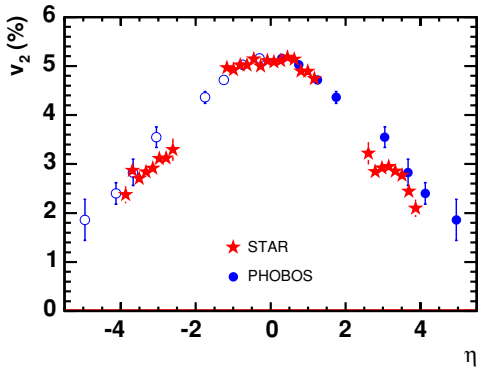

FIG. 15. (Color online) Charged-hadron v_2 vs. η at $\sqrt{s_{NN}} = 200$ GeV for STAR minimum bias (stars) and PHOBOS [29] midcentral (15–25%) centrality (circles). The open circles are PHOBOS data reflected about midrapidity.

to the true reaction plane orientation and, hence, are a source of nonflow effects. A multiparticle cumulant analysis, which has been shown to suppress nonflow effects, may give lower v_2 values because of the opposite sensitivity of $v_2\{2\}$ and $v_2\{4\}$ to the fluctuations of v_2 itself described in Sec. V B and Ref. [39].

Figure 18 shows the differential elliptic flow v_2 obtained with the standard and modified reaction plane methods as a function of p_t for different collision centralities. The modified event plane method excludes particles within $|\Delta\eta| < 0.5$ around the highest p_t particle. For both methods v_2 rises linearly up to $p_t = 1$ GeV/c and then deviates from a linear rise and saturates for $p_t > 3$ GeV/c for all centralities. Figure 9 shows a similar behavior. Although the statistical errors are large, we observe a systematic difference in Fig. 18 for the v_2 values obtained with the two methods at high transverse momenta. This is better illustrated in Fig. 19, where we show the ratio of v_2 obtained with the standard and modified reaction plane methods. At low transverse momenta ($p_t < 2$ GeV/c), the v_2 values are very similar for both methods. At higher transverse momenta, v_2 is systematically larger for the standard reaction plane method. For more peripheral collisions this

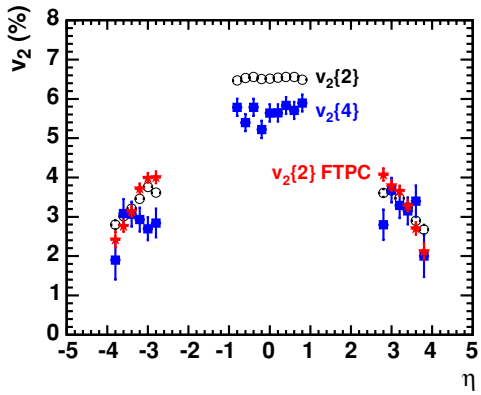

FIG. 16. (Color online) Charged hadron v_2 vs. η for 20–70% centrality collisions, including the FTPC regions. The open circles are $v_2\{2\}$, the filled squares are $v_2\{4\}$ and the stars are $v_2\{2\}$ for only FTPC particles, not using the main TPC particles.

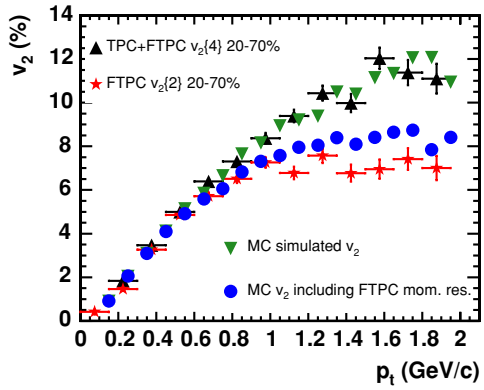

FIG. 17. (Color online) Charged hadron $v_2\{2\}$ vs. p_t for centrality 20–70% in the FTPC ($2.5 < |\eta| < 4.0$) regions (stars) compared to $v_2\{4\}$ in the TPC + FTPCs (up-triangles). The down-triangles are Monte Carlo results fit to the up-triangles, and the solid circles include the FTPC momentum resolution.

effect is larger, and it also begins at lower p_t. The modified reaction plane method seems to eliminate at least some of the nonflow effects at high transverse momenta (up to 15–20% at $p_t = 5$–6 GeV/c in the most peripheral collisions). The contribution of the azimuthal correlations not related to the reaction plane orientation has been previously studied using $p+p$ collisions [6]. In $p+p$ collisions, all correlations are considered to be of nonflow origin. In Fig. 12 the azimuthal correlations in midcentral Au+Au collisions are very different from those in $p+p$ collisions in both magnitude and p_t dependence. Figure 20 shows the modified reaction plane results on $v_2(p_t)$ for charged hadrons of centrality 20–60%. We find a very good agreement of v_2 from the modified reaction plane analysis with the two-particle cumulant results after subtracting the correlations measured in $p+p$ collisions [6]. Neither of these modified methods that seem to be necessary at high p_t give results that differ from the simple standard

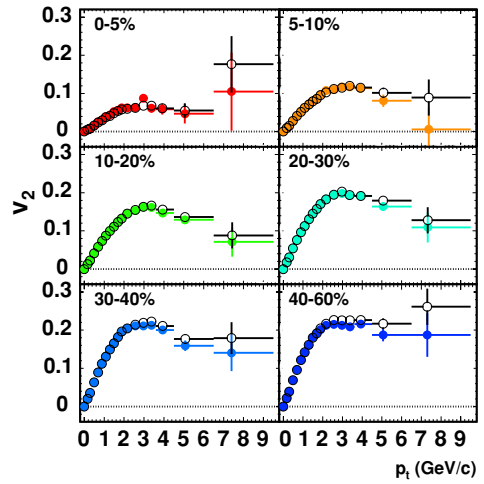

FIG. 18. (Color online) v_2 vs. p_t for charged hadrons for different centrality bins. The standard reaction plane method is shown by open symbols and the modified reaction plane method by solid symbols.

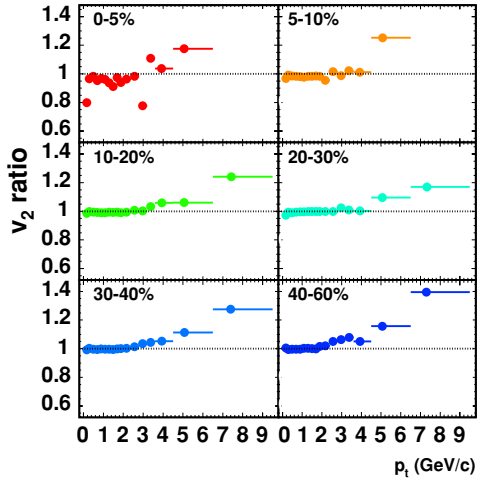

FIG. 19. (Color online) v_2 for the standard reaction plane method divided by v_2 for the modified reaction plane method vs. p_t for charged hadrons in different centrality bins. Error bars are not shown as the same data set is used for both methods.

method below p_t of 2 GeV/c and thus are not used in the other analyses of this article.

C. Higher harmonics

1. The central region

Our results for charged hadron v_4 and v_6 from this study have already been published [23,26], and $v_4(p_t)$ is shown again in Fig. 21. It also was found that v_4 scales as v_2^2. The value of v_4/v_2^2 was found to be 1.2, almost independent of p_t [26], as can be seen in the ratio graph of Fig. 22(b).

Kolb [40] pointed out that for large v_2 the azimuthal shape in momentum space described by the v_n Fourier expansion is no longer elliptic but becomes "peanut" shaped. Using our high-p_t plateau experimental values, we show this in Fig. 23. Kolb also gives an equation for the amount of v_4 needed to just eliminate the peanut waist. Figure 21 shows that the experimental v_4 values considerably exceed this value.

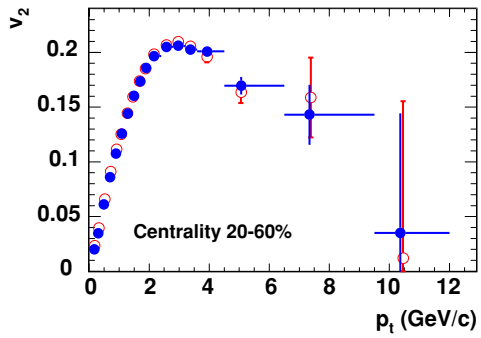

FIG. 20. (Color online) v_2 vs. p_t for charged hadrons from the modified reaction plane method (solid circles). Open circles (from Ref. [6], Fig. 2) are the two-particle cumulant results after subtracting the correlations measured in $p+p$ collisions. Error bars show statistical uncertainties only.

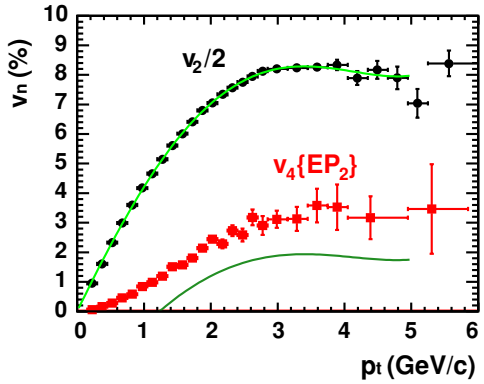

FIG. 21. (Color online) v_2 scaled down by a factor of 2, and $v_4\{\mathrm{EP}_2\}$ vs. p_t for charged hadrons from minimum bias events. Using a fit to the v_2 values, the lower solid line is the predicted v_4 needed to just remove the "peanut" waist (see text).

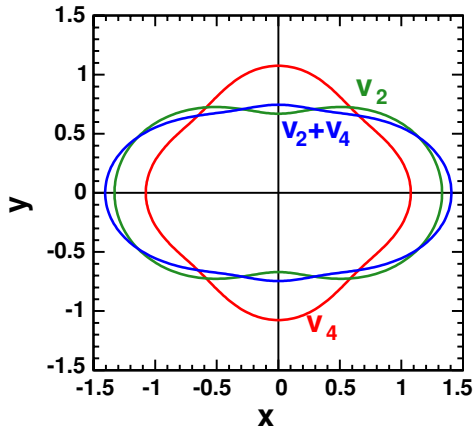

FIG. 23. (Color online) A polar graph of the distribution $1 + 2v_2\cos(2\phi) + 2v_4\cos(4\phi)$, where ϕ is the azimuthal angle relative to the positive x axis. Plotted are the distributions for $v_2 = 16.5\%$ showing the waist, $v_4 = 3.8\%$ having a diamond shape, and both coefficients together.

Figure 24 shows the $v_4\{\mathrm{EP}_2\}(p_t)$ values for the individual centralities with filled elliptic cylinder blast-wave fits assuming all charged hadrons have the mass of a pion.

Using the probability PID method [12,13] for charged pions and antiprotons, and a topological analysis method for K^0_S and $\Lambda + \overline{\Lambda}$, we obtain the $v_4\{\mathrm{EP}_2\}(p_t)$ and $v_2(p_t)$ values shown in Fig. 25. For pions the v_2^2 scaling ratio is shown in Fig. 26. To make this graph it was necessary to combine data points to get reasonable errors bars for the ratio because the v_4 values are so small. The resulting scaling ratio is consistent with that for charged hadrons shown in Fig. 22(b).

2. *The forward regions*

In Fig. 27 the fourth-harmonic $v_4\{\mathrm{EP}_2\}$ shows an average value of $(0.4 \pm 0.1)\%$ in the pseudorapidity coverage of the TPC ($|\eta| < 1.2$). In contrast, its value of $(0.06 \pm 0.07)\%$ in the forward regions is consistent with zero, with a 2σ upper limit of 0.2%. Therefore the relative falloff of v_4 from $\eta = 0$ to $\eta = 3$ appears to be stronger than for v_2. This behavior is consistent with $v_4 \propto v_2^2$ scaling.

3. *High p_t*

It has been emphasized that v_4 has a stronger potential than v_2 to constrain jet-quenching model calculations [40]. Following the same procedure as described in Ref. [6], we plot in Fig. 28 the $v_4\{3\}$ from moderately high p_t. It should be noted that the two most peripheral points go up rather than down as they do for v_2, in apparent violation of v_4/v_2^2 scaling at this high p_t. We compare the results with the fourth-harmonic anisotropy generated by energy loss in a static medium with a Woods-Saxon density profile, hard sphere (step function in density), and the extreme case: hard shell limit. The results are shown in Fig. 28. The dashed curve corresponds to the hard shell; the upper and lower bands correspond to a parametrization of jet energy loss where the absorption coefficient is set to match the suppression of the inclusive hadron yields. The lower and upper boundaries of the bands around $b = 11$ fm correspond to an absorption that gives suppression factors of 5 and 3, respectively. Note that compared to the case of v_2 [6], the calculations are less sensitive to the suppression factors (narrow bands). These model calculations cannot reproduce the correct sign of v_4 over the whole range of impact parameters and neither can they reproduce the magnitude of v_4. A similar observation was made for the magnitude of v_2 in this p_t range in Ref. [6]. In the present case, evidently the absorption of jet particles is not the dominant mechanism for producing v_4 in this p_t range.

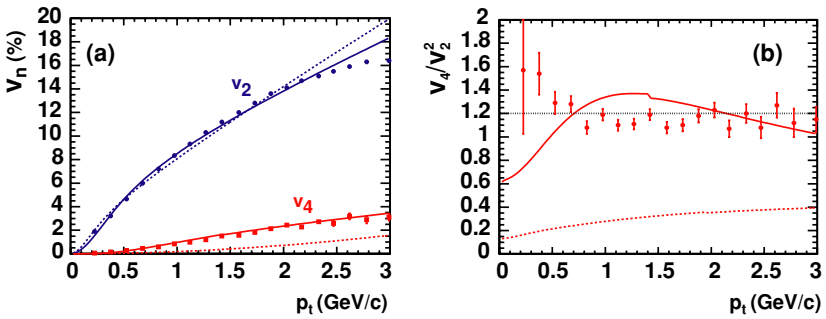

FIG. 22. (Color online) Graphs of v_n and v_4/v_2^2. The dashed lines are surface shell blast-wave fits with no ρ_4 or s_4 terms (see Sec. VI D) to the charged hadron v_2 minimum bias data. The resultant ratio v_4/v_2^2 is shown as the lower dashed line in the ratio graph (b). The solid lines are the fits with the addition of ρ_4 and s_4. The resultant ratio v_4/v_2^2 is shown as the solid curve in the ratio graph (b). The dotted line in the ratio graph (b) at 1.2 represents the average value of the data.

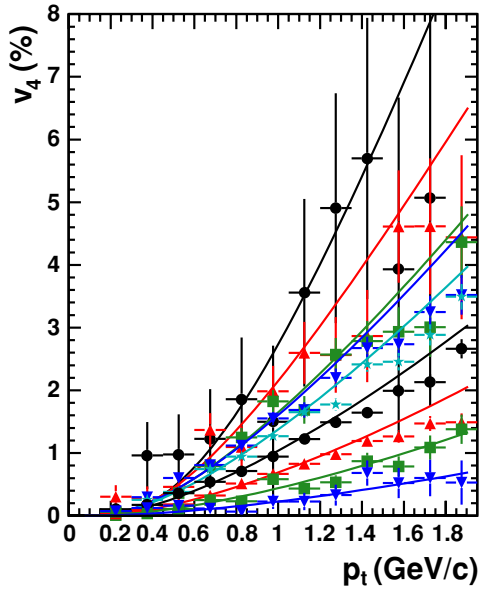

FIG. 24. (Color online) $v_4\{\mathrm{EP}_2\}$ vs. p_t for charged hadrons for the 5–10% centrality bins (bottom to top) and in steps of 10% starting at 10, 20, 30, 40, 50, 60, and 70 up to 80%. The solid lines are blast wave fits.

V. METHODS COMPARISONS

In addition to the standard and scalar product methods already described, there are also several subevent methods where each particle is correlated with the event plane of the other subevent. If the subevents are produced randomly, we call this the random subs method. If the particles are sorted according to their pseudorapidity, we call it the eta subs method. In these methods, because only half the particles are used for the event plane, the statistical errors are approximately $\sqrt{2}$ larger, but autocorrelations do not have to be removed because the particle of interest is not in the other subevent.

Another method involves fitting the distribution of the lengths of the flow vectors normalized by the square root of the multiplicity as follows [22,41,42]:

$$q_n = Q_n/\sqrt{M} \tag{7}$$

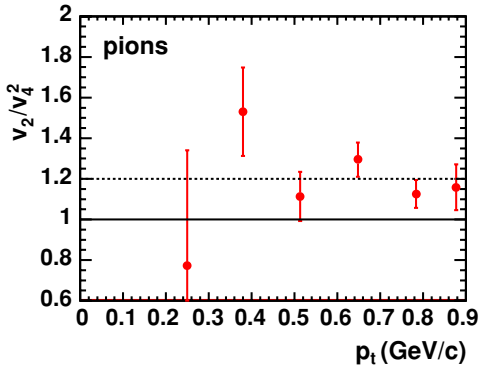

FIG. 26. (Color online) The ratio v_4/v_2^2 vs. p_t for identified pions. The dashed line is at $v_4/v_2^2 = 1.2$.

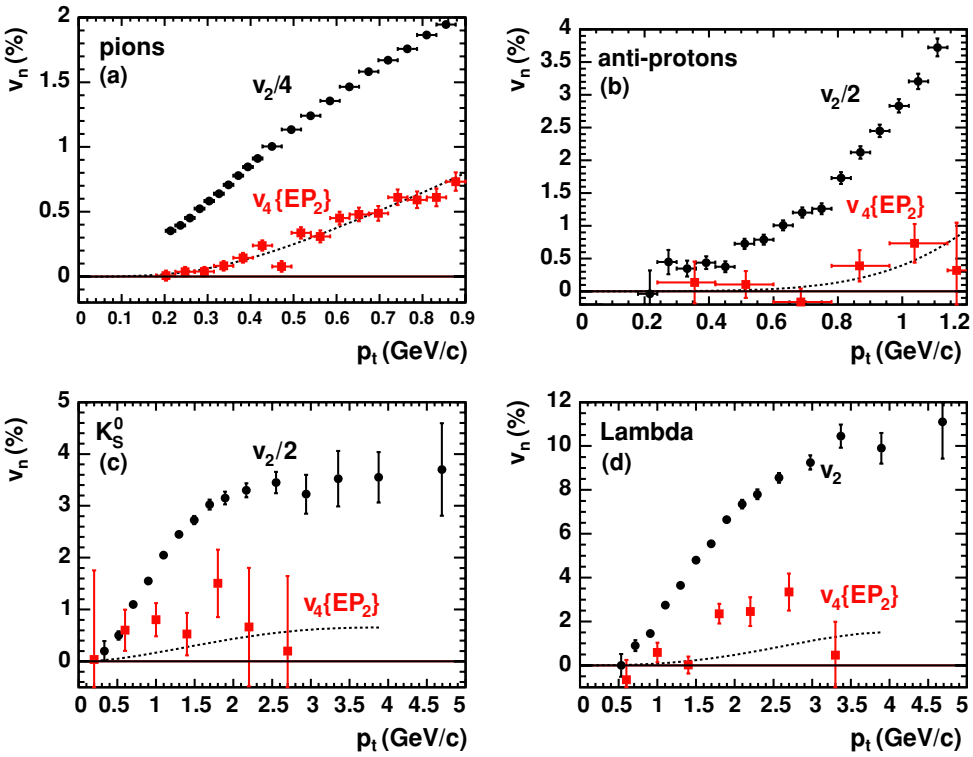

FIG. 25. (Color online) $v_4\{\mathrm{EP}_2\}$ and v_2 vs. p_t for identified pions, antiprotons, K_S^0, and $\Lambda + \overline{\Lambda}$ for minimum bias collisions. The dashed lines are at $1.2v_2^2$.

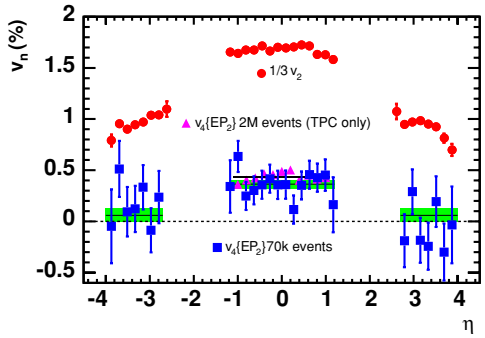

FIG. 27. (Color online) Comparison of v_2 to $v_4\{\mathrm{EP}_2\}$ for charged hadrons from minimum bias collisions as a function of pseudorapidity. The fourth harmonic (squares) is consistent with zero at forward pseudorapidities but not at midrapidity. v_2 is shown by circles, scaled by a factor of 1/3 to fit on the plot. The larger data set available for the TPC only (triangles) confirms our measurement of $v_4\{\mathrm{EP}_2\}$ at midrapidities.

$$\frac{dP}{q_n dq_n} = \frac{1}{\sigma_n^2} e^{-\frac{v_n^2 M + q_n^2}{2\sigma_n^2}} I_0\left(\frac{q_n v_n \sqrt{M}}{\sigma_n^2}\right), \tag{8}$$

where I_0 is the modified Bessel function and

$$\sigma_n^2 = 0.5(1 + g_n). \tag{9}$$

Nonflow effects are fit with the parameter g_n. The values of M are in Table II.

A. Comparisons

To make a precise comparison of the various methods we have calculated v_2 integrated over p_t and η for the main TPC and plotted it vs. centrality in Fig. 29(a). To make the comparison valid we have used the same events and the same cuts, which are shown in Table I. The integrated values have not been corrected for the missing regions beyond the integration limits given. The systematic error at the lowest p_t values ($\approx$0.2 GeV/c) is probably larger than at higher p_t, but its contribution to the integrated v_n values is small because the yield is so low there. For constructing the Q vector, linear p_t weighting was used for all methods except the q distribution method, where no weighting was used. From the agreement of different software implementations of the same method, we estimate a relative systematic error (not included) of at least 2% of the v_2 values shown.

The results fall generally into two bands: those for two-particle correlations methods and those for multiparticle methods. The difference is because of either the decreased sensitivity of the multiparticle methods to nonflow effects or to their increased sensitivity to fluctuation effects [39]. Thus, the "true" flow values must be between these two limits. To expand the graph to look for small differences we also have plotted the ratios to the standard method in Fig. 29(b). It appears that the standard method is about 5% lower than the other two-particle correlation methods. We first thought that this might be because of nonflow effects affecting the extrapolation in the standard method from the subevent resolution to the full event resolution. However, it also could be because of the fact that the standard method uses twice as many particles as the subevent methods and therefore is less sensitive to nonflow effects. But this does not explain why the scalar product method falls in the band with the subevents. The values from the eta subevent method decrease for peripheral collisions. This could be because of decreased nonflow effects for particles separated in pseudorapidity.

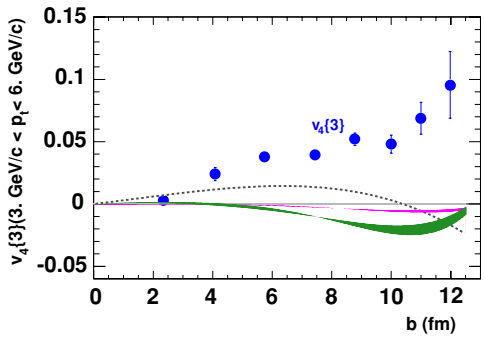

FIG. 28. (Color online) High p_t charged hadron $v_4\{3\}$ integrated for $3 \leqslant p_t \leqslant 6\,\mathrm{GeV}/c$ vs. impact parameter b, compared to models of particle absorption: dashed curve is the hard shell, higher narrow band is Woods-Saxon, lower wider band is hard sphere. The bands have widths for absorption to match the observed range of yield suppression.

B. Nonflow effects and fluctuations

Particle correlations that are not correlated with the reaction plane are called nonflow effects when they affect v_n. Figure 30 shows the two- four- and six-particle integral cumulant v_2 values using the cuts in Table I. The four- and six-particle results agree, showing that nonflow effects are eliminated already with four-particle correlations.

Nonflow can be calculated by the difference between the squares of the two-particle and four-particle cumulant v_2 values, normalized with the number of wounded nucleons from Table II. Thus [22,27,65] we have the following:

$$g_2 = N_{\mathrm{WN}} \times \left(v_2^2\{2\} - v_2^2\{4\}\right), \tag{10}$$

which is shown in Fig. 31 for $\sqrt{s_{NN}} = 200$ GeV, 130 GeV, and from the SPS at 17.2 GeV [65]. The SPS g_2 values were divided by the multiplicity used and multiplied by N_{WN}, both given in that article [65]. From the q distribution method of calculating v_2, g_2 can be obtained by the increase in the width of the distribution from Eq. (9). (It should be pointed out that in these fits, v_2 and g_2 are somewhat anticorrelated.) For the q distribution method the g_2 values were also divided by the multiplicity used and multiplied by N_{WN}. Thus, all four results have been renormalized to use the number of wounded nucleons. Instead of being independent of centrality as originally thought, g_2 seems to decrease somewhat for the more peripheral collisions but appears to have the same shape for all the systems. The results for 17 GeV may be different from the others because g_2 could vary with the acceptance of the detector. At 200 GeV it is possible that g_2 from the

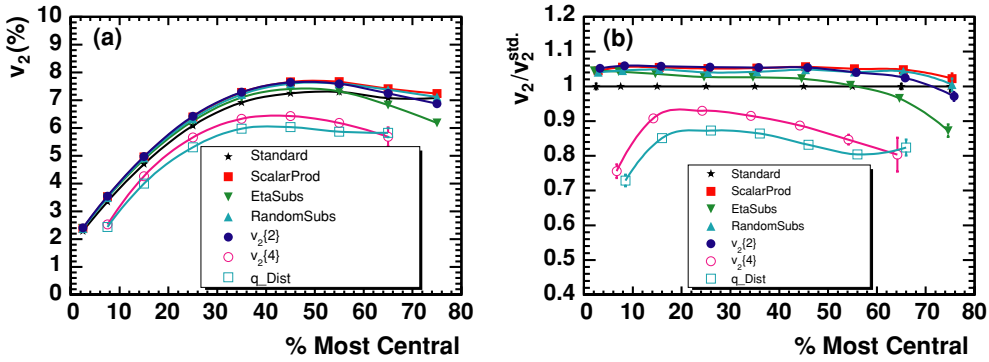

FIG. 29. (Color online) Charged-hadron v_2 integrated over p_t and η vs. centrality for the various methods described in the text. (b) The ratio of v_2 to the standard method v_2.

q distribution method is larger than from the cumulant method because of real fluctuations in v_2 broadening the q distribution. Although the definition of q in Eq. (7) removes most of the multiplicity dependence of Q, Eq. (8) still contains the quantity M, and thus is subject to the spread in M in a centrality bin.

Fluctuations of the true v_2 can lead to an increase in the $v_2\{2\}$ values and an equal decrease in the $v_2\{4\}$ values [22]. In Ref. [39] initial spatial eccentricity fluctuations are calculated in an MCG model and their possible effect on the determination of elliptic flow is estimated. To do this they take

$$(\varepsilon\{2\})^2 = \langle\varepsilon^2\rangle$$
$$(\varepsilon\{4\})^4 = 2\langle\varepsilon^2\rangle^2 - \langle\varepsilon^4\rangle,$$

where the averages are over events and ε is the eccentricity that will be defined in Eq. (15). The physics assumption is that $v_2 \propto \varepsilon$. Figure 32 top panel shows $\varepsilon\{4\}/\varepsilon\{2\}$ for the quark and nucleon MCG. As with nonflow, this ratio is smaller than unity over the whole centrality range, with the largest suppression for the nucleon MCG. The data for 130 [22] and 200 GeV are in between the calculated values and are closer to the nucleon (quark) MCG results for peripheral (central) collisions. When the fluctuations are small it can be shown that $v_2\{4\} \approx v_2\{6\}$, and from Fig. 30 it is clear that the data indeed support this.

Figure 32 bottom panel shows the calculated g_2 because of eccentricity fluctuations [39]. In contrast to expectations from nonflow, which would predict a constant value of g_2 vs. centrality, the eccentricity fluctuations reproduce the observed drop of about a factor 3 vs. centrality as observed in the data.

Thus it appears that either nonflow or fluctuations can explain the two bands in Fig. 29. Most probably it is some of both. Because nonflow effects and fluctuations raise the two-particle correlation values, and fluctuations lower the multiparticle correlation values, the truth must lie between the lower band and the mean of the two bands. At the moment we can only take the difference of the bands as an estimate of our systematic error.

VI. MODEL COMPARISONS

This section compares the experimental results with model calculations. Measurements of event anisotropy, especially elliptic flow v_2, are sensitive to the early collision dynamics [43–46]. Extracting physics from the huge set of presented data is done via a variety of methods, ranging from transport models that include really quite detailed (and diverse) descriptions of the subnuclear dynamics to hydrodynamic models that make simplifying assumptions (zero mean free path and thermalization) rendering all dynamic details irrelevant and focusing all physics on the equation of state. We first consider schematic concepts such as coalescence that propose an underlying nature of the flowing constituents and allow observable tests of scaling relations implied by those concepts. Finally we

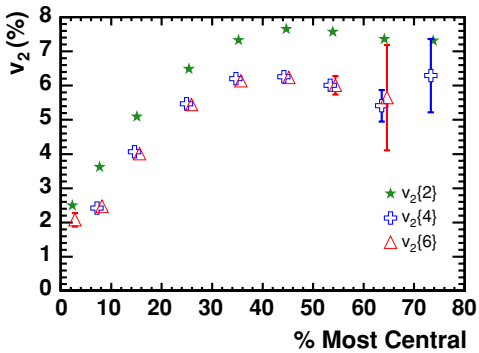

FIG. 30. (Color online) Charged hadron $v_2\{2\}$, $v_2\{4\}$, and $v_2\{6\}$ integrated values as a function of centrality.

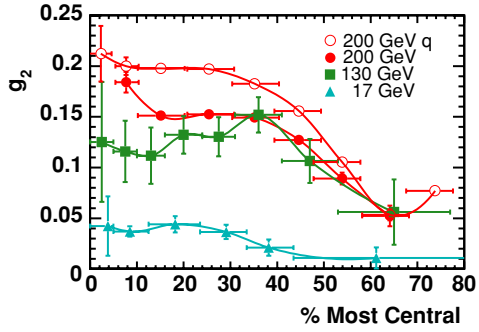

FIG. 31. (Color online) The nonflow parameter, g_2, as a function of centrality. The solid points are from the cumulant method. The open circles are from the q distribution method.

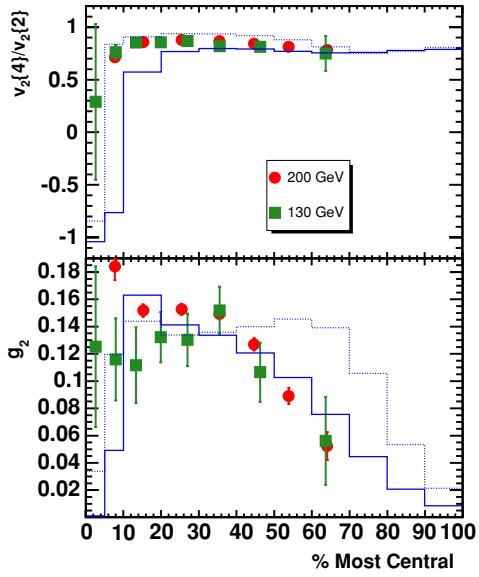

FIG. 32. (Color online) (Upper panel) The ratio $v_2\{4\}/v_2\{2\}$ for charged hadrons as a function of centrality. The lines are a Monte Carlo Glauber model calculation of $\varepsilon_2\{4\}/\varepsilon_2\{2\}$. (Lower panel) The nonflow parameter, g_2, as a function of centrality. The lines are a Monte Carlo Glauber model calculation of $N_{\mathrm{WN}}(v_2/\varepsilon)^2(\varepsilon_2^2\{2\} - \varepsilon_2^2\{4\})$. In both panels the solid lines assume nucleons, whereas the dotted lines assume quarks.

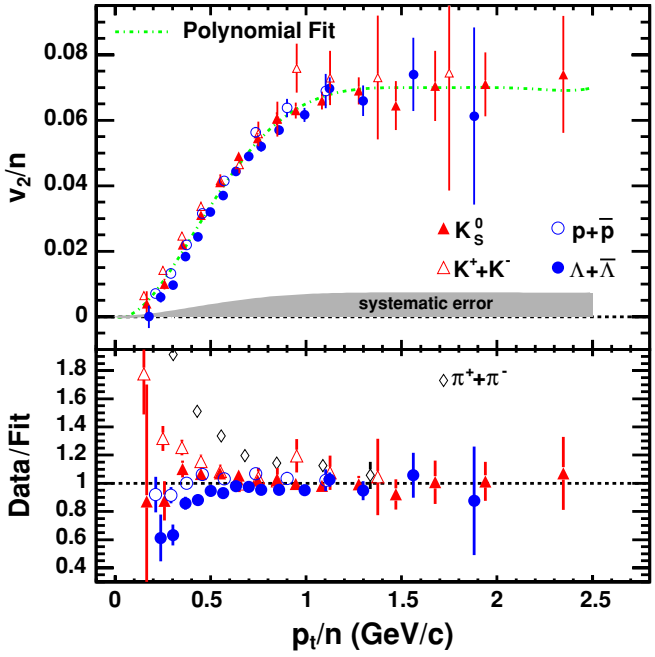

FIG. 33. (Color online) (Top panel) Identified particle v_2 from minimum bias collisions. The vertical axis and horizontal axis have been scaled by the number of constituent quarks (n). Pions are not plotted. A polynomial curve is fit to the data. The possible systematic error is indicated by the gray band. (Bottom panel) The ratio of v_2/n to the fitted curve.

use a simple blast-wave parametrization, which tries to see whether a consistent picture of all data can be achieved and to identify what are the required driving features (like geometric anisotropy at freeze-out, etc).

A. Coalescence of constituent quarks

Models of hadron formation by coalescence or recombination of constituent quarks successfully describe hadron production in the intermediate p_t region ($1.5 < p_t < 5$ GeV/c) [20,30,47]. These models predict that at intermediate p_t, v_2 will approximately scale with the number of constituent quarks (n) with v_2/n vs. p_t/n for all hadrons falling on a universal curve. When hadron formation is dominated by coalescence, this universal curve represents the momentum-space anisotropy of constituent quarks prior to hadron formation. This simple scaling, however, neglects possible higher harmonics and possible differences between light and heavy quark flow.

Figure 33 (top panel) shows v_2 vs. p_t for the identified particle data of Fig. 10, where v_2 and p_t have been scaled by the number of constituent quarks (n). A polynomial function has been fit to the shown scaled values. To investigate the quality of agreement between particle species, the data from the top panel are scaled by the fitted polynomial function and plotted in the bottom panel. For $p_t/n > 0.6$ GeV/c, the scaled v_2 of K^0_S, $K^{\pm}$, $p + \bar{p}$, and $\Lambda + \overline{\Lambda}$ lie on a universal curve within statistical errors. The pion points, however, deviate significantly from this curve even above 0.6 GeV/c. This deviation may be caused by the contribution of pions from resonance decays [48]. Alternatively, it may reflect the difficulty of a constituent quark coalescence model to describe the production of pions whose masses are significantly smaller than the assumed constituent quark masses [30].

At the end of Sec. V B we estimated that the v_2 values from two-particle correlations could be systematically high by between about 10 to 20%. This was based on the integrated values for charged particles and we do not know yet how this varies with p_t and particle type. However, to indicate this estimated systematic error a shaded band of 10% is shown in Fig. 33 (top panel).

The v_2/n of $\pi^{\pm}$, $\bar{p}$, K^0_S, and $\Lambda + \overline{\Lambda}$ from three centrality intervals are shown in the top panels of Fig. 34. The K^0_S and $\Lambda + \overline{\Lambda}$ values are from Ref. [20]. In the bottom panels, the ratios to the fitted curves are shown. The most central data (0–5%) are thought to be affected by nonflow correlations (see Sec. V). For the 30–70% and 5–30% centrality intervals, the v_2 of $\bar{p}$, K^0_S and $\Lambda + \overline{\Lambda}$ agree with constituent quark number scaling for the expected p_t/n range above 0.6 GeV/c to within 10%.

Figure 10 showed that the data for the heavier baryons seem to cross over the data for the mesons at sufficiently high p_t. The data in Fig. 8 are consistent with this. In the low p_t region the heavier particles have lower v_2 values as expected for the mass ordering from hydrodynamics. In the intermediate p_t coalescence plateau region the three quark baryons have a larger v_2 than the two quark mesons. Thus the experimentally observed crossover is thought to be because of a change in the particle production mechanism.

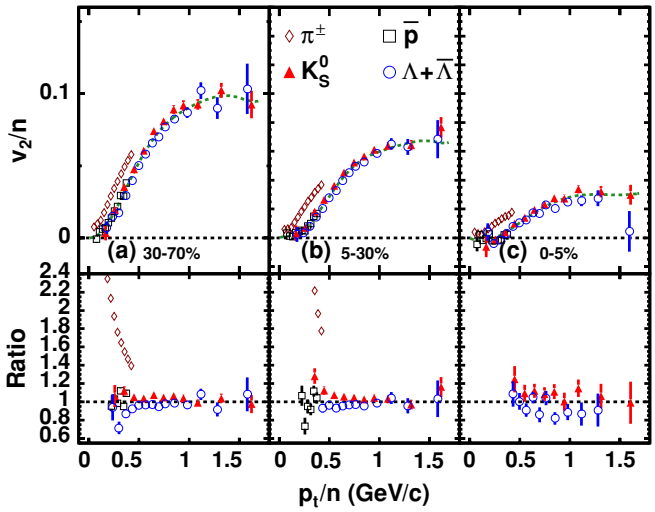

FIG. 34. (Color online) (Top panels) The v_2 of $\pi^{\pm}$, $\bar{p}$, K^0_S, and $\Lambda + \overline{\Lambda}$ from three centrality bins (30–70%, 5–30%, and 0–5% of the collision cross section) scaled by the number of constituent quarks (n) vs. p_t/n. Polynomial curves are fit to the data excluding the pions. (Bottom panel) The ratios of v_2/n to the fitted curves.

From a simple parton coalescence model one can calculate [49] the observed v_4/v_2^2 scaling ratio in terms of the same quantity for the quarks. The relationships between meson (M) or baryon (B) v_4/v_2^2 and quark (q) v_4/v_2^2 are as follows:

$$\left[v_4/v_2^2\right]^M_{p_t} \approx 1/4 + (1/2)\left[v_4/v_2^2\right]^q_{p_t/2}, \tag{11}$$

and

$$\left[v_4/v_2^2\right]^B_{p_t} \approx 1/3 + (1/3)\left[v_4/v_2^2\right]^q_{p_t/3}. \tag{12}$$

These can be rearranged [49] to relate v_4/v_2^2 for mesons and baryons as follows:

$$\left[v_4/v_2^2\right]^B_{p_t/3} \approx (2/3)\left[v_4/v_2^2\right]^M_{p_t/2} + 1/6. \tag{13}$$

The observed v_4/v_2^2 scaling ratios, which appear to be fairly independent of p_t in Figs. 22(b), 25, and 26, are shown in Table III. Although in Fig. 33, quark-number scaling is shown to work within errors at $p_t/n > 0.6\,\text{GeV}/c$ for all particles except pions, it appears that v_4/v_2^2 scaling may be applicable over a wider range of p_t. Charged hadrons are in the table but should be used with care because they represent a complicated superposition of baryons and mesons from different values of p_t/n where the B/M ratio is strongly dependent on centrality and we cannot even assume that the values are a good estimator for mesons. The kaon values are not accurate enough to test the above equation. Even though the pions are known to deviate from the constituent quark number coalescence predictions, we can calculate with Eq. (13), from the charged pions for the wide p_t range, that v_4/v_2^2 for baryons should be 0.96 ± 0.03. This is compatible with the values for antiprotons and $\Lambda + \overline{\Lambda}$ in Table III. Equation (13) would be valuable for testing the concept of quark coalescence in an equilibrated medium, but the accuracy of the data so far do not allow a conclusion.

TABLE III. The ratio v_4/v_2^2 for all p_t and only for $p_t/n > 0.6\,\text{GeV}/c$.

	All p_t	$p_t/n > 0.6\,\text{GeV}/c$
$h^{\pm}$	1.17 ± 0.01	1.14 ± 0.02
$\pi^{\pm}$	1.19 ± 0.04	
K^0_S	3.1 ± 1.2	2.5 ± 1.3
$\bar{p}$	1.46 ± 0.53	
$\Lambda + \overline{\Lambda}$	0.97 ± 0.18	0.87 ± 0.22

If, in addition, one assumes [49,50] that the scaling relation for the partons is as follows:

$$v_4^q = \left(v_2^q\right)^2, \tag{14}$$

then from Eq. (11) $v_4/v_2^2 = 1/4 + 1/2 = 3/4$. For baryons this ratio from Eq. (12) is $1/3 + 1/3 = 2/3$, which is even smaller. But, one can see in Table III that experimentally this ratio is close to 1.2 for charged hadrons and pions, so that either the parton scaling relation [Eq. (14)] must have a proportionality constant of about 2, or the simple coalescence model needs improvement.

B. Transport models

Most of the transport model analyses were done for charged hadrons, but we will only compare some of the models with identified hadrons. Microscopic hadronic transport calculations underpredict the absolute amplitude of v_2 by a factor of 2 to 3. However, most of the observed features, such as mass hierarchies in both the low p_t region and the meson-baryon order, are seen in hadron transport model calculations [51]. The strength of v_2 should be sensitive to the density and interaction frequency of the constituents. Indeed, when reducing the hadron formation time, the v_2 values are found to increase [51]. In addition, the tests with the parton cascade models AMPT [52] and ZPC [53] give the correct mass hierarchy but require a large parton cross section to mimic the early development of v_2 at midrapidity. In ultrarelativistic nuclear collisions, hadrons may not be the right degrees of freedom to describe the early dynamics. At large values of pseudorapidity, however, the AMPT [54] model seems able to describe the v_1, v_2, and v_4 results without the large parton cross sections and string melting. At all pseudorapidities, at the later stage, when particle density becomes dilute, transport effects will become important [55,56].

For v_4 the parton cascade model AMPT [50] with string melting and a large parton cross section, does calculate reasonable values. However, the calculated proportionality constant in Eq. (14) is about 1, whereas our data with a simple coalescence model [30] imply it to be about 2.

C. Hydrodynamic models

Azimuthal momentum anisotropies in the final state are generated by particle reinteractions from azimuthal spatial anisotropy in the initial state. In the hydrodynamic framework, these reinteractions are modeled by assuming zero mean

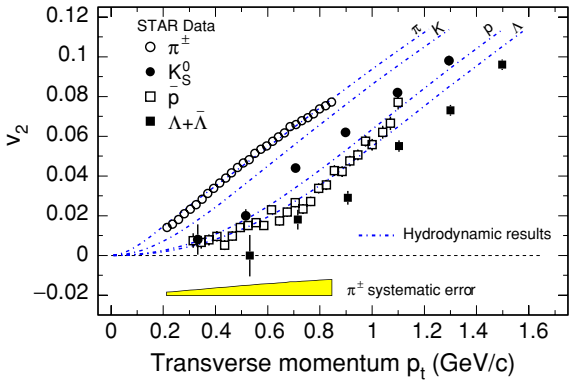

FIG. 35. (Color online) $v_2(p_t)$ for charged π, K^0_S, $\bar{p}$, and $\Lambda + \overline{\Lambda}$ from minimum bias collisions. Hydrodynamic calculations [31,60] are shown as dot-dashed lines. The possible systematic error is shown at the bottom.

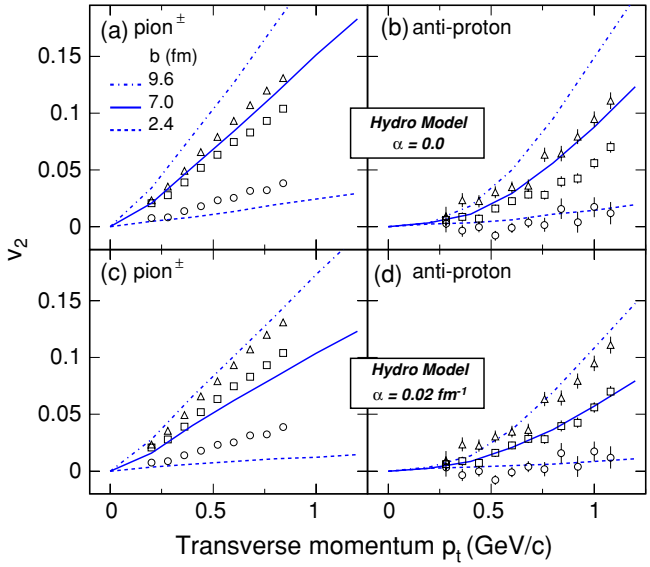

FIG. 36. (Color online) Charged π plots on the left and $\bar{p}$ plots on the right for v_2 for three centrality bins are shown as a function of p_t. The data are from centralities 40–50% (open triangles), 20–30% (open squares), and 0–5% (open circles). The corresponding results of a hydrodynamic calculation are shown as dot dashed lines, solid lines, and dashed lines, respectively. Plots on the top are for $\alpha = 0$ and plots on the bottom are for $\alpha = 0.02\,\mathrm{fm}^{-1}$. Here α determines the initial velocity kick for the hydrodynamic model calculation [61].

free-path and therefore local thermalization. Hydrodynamic calculations have been successful at reproducing previously published data on v_2 and spectra [57–59].

Hydrodynamic calculations have been shown in Figs. 6, 8, 9, and 10, with reasonable agreement with the v_2 and $v_2\{4\}$ data up to p_t of 1–2 GeV/c. Additional results for v_2 at low p_t from minimum bias collisions are shown in Fig. 35. Results of K^0_S and $\Lambda + \overline{\Lambda}$ are from Ref. [20]. The hydrodynamic calculations [31,57,60] are consistent with the experimental results considering the systematic errors, such as the matching of the centralities are not included. Also, as described in Sec. V, the data could be 10 to 20% systematically high. To indicate this in the plot a band of 10% of the charged pions is shown. The characteristic hadron mass ordering of v_2 is seen in the low p_t region, where at a given p_t, the higher the hadron mass the lower the value of v_2. This supports the hypothesis of early development of collectivity and possible thermalization in collisions at RHIC [57,59], although the underlying mechanism for the equilibration process remains an open issue.

As seen in Fig. 33 the observed values of v_2 saturate and the level of the saturation seems dependent on the number of constituent quarks (n) in the hadron. The saturation value is about $0.07n$ for $p_t/n > 1$ GeV/c. Hydrodynamic calculations do not saturate in this p_t region.

Figure 36 shows the centrality dependence of pion and antiproton v_2 compared with hydrodynamic results [61]. The three centrality bins shown are described in Table II. Systematic uncertainties, such as the matching of the centralities, are not included. Also, from the Fig. 29(b) ratio graph in Sec. V it can be seen that the 0–5% centrality data could be 25% high. An important concern for the 0–5% centrality bin is the fluctuations. Just averaging over the spread in impact parameters in this bin could lower v_2 a factor of two [22,39]. In the hydrodynamic calculation, the decoupling temperature was set to 100 MeV. To fit the p_t spectra of (anti-)protons, the hydrodynamic evolution was started with an initial transverse velocity kick of $\tanh(\alpha r)$, where α is a parameter [61]. The results for v_2 are shown in Fig. 36. For $\alpha = 0$, Figs. 36(a) and (b), neither pion nor antiproton results can be fitted. For $\alpha = 0.02\,\mathrm{fm}^{-1}$, antiproton (d) v_2 can be fitted reasonably well but, for pions (c), the model results still miss the data. It appears that with the initial velocity, there is too much kick for pions at both midcentral and central collisions. Because of their light mass, perhaps pions decouple from the system relatively earlier than protons, as also indicated in the pion interferometry results [62]. It seems that for the 40–50% centrality data the hydro calculations overpredict the data, which is not surprising for peripheral collisions.

Both Hirano [63] and Heinz and Kolb [64] explain the falloff of v_2 at high η as being because of incomplete thermalization. The particle density, dN/dy, also falls off in the same way, and at high η is similar to that at midrapidity at the SPS [65], where the flow values are also lower. Possibly, the lower particle density leads to less thermalization and therefore smaller v_2 values.

Hydrodynamic inspired fits have been done for spectra [66]. Csanád *et al.* now report results where the authors claim that the resulting p_t spectra, interferometry parameters, and anisotropy can all be fitted [67]. In particular, they have a falloff of v_2 at high η. But their $v_1(\eta)$ has a large wiggle near midrapidity that is not observed. They further determined the source parameters and concluded that about 15% of the hadrons are emitted directly from the superheated region.

So far there have been very few model calculations of v_4. However, the magnitude and even the sign of v_4 are more sensitive than v_2 to initial conditions in the hydrodynamic calculations [40]. This calculation predicted v_4/v_2^2 to vary from 0.7 to 0.3 going from low to high p_t, which is about a factor of 2 lower than observed in the Fig. 22(b) ratio graph and

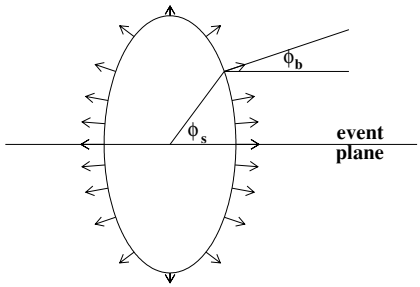

FIG. 37. Schematic illustration of an elliptical subshell of the source. Here, the source is extended in the direction out of the event plane ($R_y > R_x$). Arrows represent the direction and magnitude of the flow boost. In this example, $\rho_2 > 0$. From Ref. [68].

Table III. This calculation also predicted a strongly negative v_6, which is not observed [23].

D. Blast-wave models

Blast-wave models parametrize the coordinate and momentum freeze-out configuration generated in hydrodynamic calculations. In a self-consistent hydrodynamic calculation, this configuration is determined by the equation of state and freeze-out prescription; in blast-wave calculations, parameters of the distribution may be varied arbitrarily to fit the data. In this sense, blast wave is a "toy" model useful mainly to characterize the data and determine the magnitude of thermal (random) motion, collective motion, geometry, and so on. The model also provides parameters that can be used to study the evolution of flow varying the initial conditions, which in this article is achieved by varying centrality.

The present article uses two versions of the blast-wave parametrization. In the first one, all particles are emitted from a surface shell boosted by a constant flow velocity [12,26]. In the second one, particles are emitted from a filled elliptic cylinder boosted perpendicular to the surface of the cylinder and with a linear transverse rapidity profile inside the cylinder [68]. In this article, unless otherwise specified, blast-wave fits have referred to the filled elliptic cylinder version.

In recent versions of blast-wave models, the system is assumed boost invariant in the beam direction. As suggested in Fig. 37 for the filled elliptic cylinder, the geometry in the transverse direction is a filled ellipse with the major axis aligned with the reaction plane or perpendicular to it. One may quantify the geometrical anisotropy of the system with following the eccentricity:

$$\varepsilon \equiv \frac{R_y^2 - R_x^2}{R_y^2 + R_x^2}, \tag{15}$$

where the x direction is in the reaction plane. Superimposed on a randomly directed energy component quantified by a temperature, T, each geometrical cell of the system is boosted "outward" by a velocity (flow) field. Here, "outward" indicates the direction normal to the surface of the elliptical shell on which the element sits. The magnitude of the flow field vanishes (by symmetry) at the center of the system and grows linearly with the distance from the center, reaching its maximum at the transverse edge of the system (here assumed to be a sharp, nondiffuse edge). The average value of the flow magnitude is quantified by a parameter ρ_0. The flow magnitude may be larger (or smaller) for sources emitting in the x versus the y direction; the magnitude of this boost oscillation with azimuthal angle is quantified by the parameters ρ_2 and ρ_4. In Fig. 37, a larger in-plane than out-of-plane boost (corresponding to $\rho_2 > 0$) is suggested by the longer boost angles in plane.

Several parameters of the system affect v_2. Obviously, the larger the magnitude of ρ_2, the larger the momentum-space anisotropy. Further, the geometric anisotropy plays a role even if the boost strength is identical in all directions ($\rho_2 = \rho_4 = 0$), if $R_y > R_x$ ($R_y < R_x$) it is clear from Fig. 37 that a greater (lesser) number of elements boost particles into the reaction plane, resulting in anisotropy in azimuthal momentum space. Finally, it is clear that the temperature, T, plays a role, because if the random energy component is dominant (T larger than the rest mass), momentum anisotropies will be reduced. An extensive discussion of the interplay between these effects may be found in Ref. [68].

To summarize, the free parameters of the fits in the shell case are T, ρ_0, ρ_2, ρ_4, s_2, and s_4, where T is the temperature parameter, the ρ_n are the harmonic coefficients of the source element boost in transverse rapidity, and the s_n are the harmonic coefficients of the source density that boosts into a particular direction. In previous parametrizations [12] where there was no ρ_4, ρ_2 was called ρ_a. In the filled ellipse case the free parameters are T, ρ_0, ρ_2, ρ_4, R_x, and R_y, where R_x is the in-plane radius of the ellipse and R_y is kept constant at a nonzero value. In fitting data with a surface shell model ρ_0 is about 2/3 as large as for a solid cylinder with a linear profile. The eccentricity is approximately equal to $2s_2$. For an ellipse, the parameter s_4 is approximately equal to s_2^2. The actual equations used are given in Appendix A.

First we verified that the hydrodynamic calculations reported in Ref. [40] can be successfully fit by the blast-wave model with reasonable parameters: $T = 93$ MeV, $\rho_0 = 0.91$, $\rho_2 = 0.080$, $\rho_4 = 0.0017$, $\varepsilon = 0.122$. Because the hydro had no error bars there is no χ^2/ndf. Although spectra and v_2 are well reproduced up to $p_t = 1.5$–2 GeV/c, the p_t dependence of v_4 appears quadratic in the blast wave, although rather linear in the hydrodynamic calculation.

We have seen in Fig. 7 that the blast-wave parametrization does a good job at simultaneously reproducing pion, kaon, and antiproton v_2. The fits are performed simultaneously to spectra as well as on v_2 and v_4, to be overconstrained. Pion, kaon, and proton spectra (not shown) are well reproduced. Because spectra have typically more data points and smaller error bars, both T and ρ_0 can be determined, whereas ρ_2, ρ_4, and ε are constrained by the v_n. The total χ^2 per degree of freedom varies for different centralities around an average value of 56/65, without exhibiting any specific dependences. The average χ^2 per data point is 14/6 for pions, 7/4 for kaons, and 17/10 for protons. When looking at individual data sets (e.g., pion v_2, proton spectra), the χ^2 is compared to the number of data points because the degrees of freedom can only be calculated including all the data points as each parameter is constrained

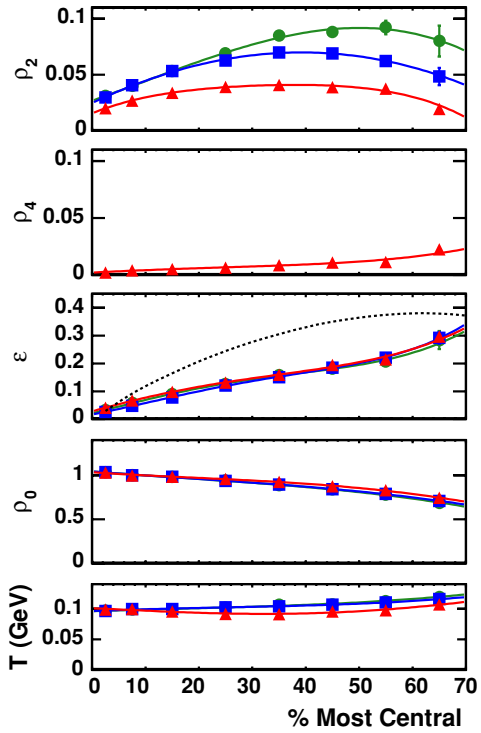

FIG. 38. (Color online) The blast-wave parameters ρ_2, ρ_4, ε, ρ_0 and T plotted vs. centrality. The circles are for pions from a two-particle cumulant analysis, the squares for pions from a standard event-plane analysis, and the triangles for charged hadrons from a standard analysis. The lines are polynomial fits. In the middle panel the initial geometrical eccentricity is also plotted as a dashed line. The actual parameter values are available at http://www.star.bnl.gov/central/publications/.

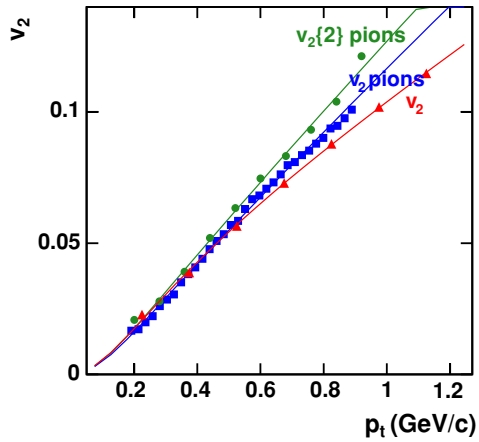

FIG. 39. (Color online) For centrality 20–30% we show $v_2\{2\}$ for pions (circles), v_2 for pions (squares), and v_2 for charged hadrons (triangles). The solid lines are blast-wave fits.

by more than one data set. Because the v_2 error bars are small (less than 5%) compared to the spectra error bars (between 5 and 10%) the total χ^2 is dominated by the contributions from the v_2 results. The calculation fits the peculiar negative values of the antiproton v_2 in Fig. 7(c) in central collisions with p_t below 0.5 GeV/c. This feature is reproduced when ρ_2 is significant whereas the thermal velocity is small. In this case the flow boost is strong enough that it suppresses the low p_t antiproton emission in plane compared to out of plane [31]. When the eccentricity is sufficiently large this phenomenon does not take place. The pion $v_2(p_t)$ data points in Fig. 7(a) are similar in the three most peripheral bins. However, the anti-proton values are not and thus meaningful fits are still possible. The p_t ranges in GeV/c used for the blast-wave fits where the data had reasonable error bars were 0.4 to 1.0 for pions, 0.15 to 0.5 for kaons, and 0.3 to 1.1 for antiprotons.

The blast-wave parameters obtained from fitting v_2 and v_4 data are shown in Fig. 38. They provide a good way to systematize a large amount of experimental data. It should be emphasized that other formulations of the blast-wave model would give different fit parameters [69]. As the parameters T and ρ_0 are constrained mostly by spectra, they agree with the values published [70]. ρ_2 and ε are fully constrained by the v_2 data. ρ_2 reaches a maximum in the centrality region 30–60%. This is easily understood recalling that in this centrality region, the initial spatial azimuthal anisotropy of the system is large, whereas the initial energy density is still large enough to trigger a significant collective expansion. This expansion is clearly visible comparing the initial and final eccentricities. The system spatial deformation is a maximum in the region where the azimuthal push quantified by ρ_2 is a maximum. Thus, the blast-wave parametrization provides an intuitive self-consistent description of the data.

For one centrality we show in Fig. 39 the charged hadron results from this standard event-plane analysis, together with pion results for a standard analysis and a two-particle cumulant analysis. As shown in Sec. V, the integrated two-particle cumulant $v_2\{2\}$ values are usually 5% higher than the standard v_2 values. The charged hadron values are somewhat smaller than the pion values, because of the presence of protons. Even though the flow values are fairly close, the ρ_2 fit parameters shown in Fig. 38 differ appreciably. This is because the ε values come out the same and the small differences in the v_2 values are all forced into the ρ_2 values. It appears that the ε values are at least half as large as the initial eccentricities of the overlap region.

Both hydrodynamic calculations and blast-wave fits can well reproduce transverse-momentum spectra and second-harmonic anisotropy (v_2). However, as mentioned above, hydrodynamic calculations do not agree with measured values of v_4. The question, then, is whether blast-wave parameters may be adjusted to simultaneously fit v_2 and v_4, hopefully providing useful feedback to theorists doing the hydrodynamic calculations. Blast-wave fits to v_4 are shown in Fig. 24.

Even with only second-harmonic anisotropies in flow strength and spatial geometry, fourth-harmonic momentum-space anisotropies (v_4) are produced in blast-wave calculations. Thus it is possible that one could generate v_4 without any fourth-harmonic anisotropy ρ_4 in Eq. (A1) [49]. Using the surface shell blast-wave model, we have fit the v_2 data using only ρ_2 and s_2 and then calculated v_4 as shown in Fig. 22 as the dashed lines. The calculated v_4 values are much

too small, indicating that a real fourth-harmonic term is necessary. Then we allowed ρ_4 and s_4 to vary as well and obtained the fits shown in Fig. 22 as solid lines. The fact that these parameters are significant suggests that the spatial distribution of the system initial state has a significant fourth-harmonic component, which translates into a fourth-harmonic flow oscillation.

VII. CONCLUSIONS

All the presently available STAR data for anisotropic flow in Au+Au collisions at $\sqrt{s_{NN}} = 200$ GeV are presented for charged particles and for identified species. Agreement between flow data for STAR and other RHIC experiments is good. New evidence confirms our earlier finding that elliptic flow is in plane at RHIC. v_2 as a function of pseudorapidity is not flat, but confirmed to be bell shaped. A detailed comparison of flow analysis methods shows that either nonflow effects or fluctuations can explain the difference between v_2 from two-particle correlation results and multiparticle correlation results. The mass dependence of v_2 at low p_t follows the pattern predicted by hydrodynamic models, but a transition to a behavior consistent with quark coalescence at higher p_t is observed. For identified particles, v_2 scales with the number of constituent quarks, n, within errors above $p_t/n \sim 0.6$ GeV/c for charged and neutral kaons, for antiprotons, and for $\Lambda + \overline{\Lambda}$ hyperons. This supports the picture of hadron production via coalescence of constituent quarks involved in collective anisotropic motion. If confirmed it would be a strong argument for the deconfinement reached in the system. Only pions deviate from this behavior, which partially can be explained by the large resonance decay contribution to pion production and by the light pion mass. For the higher flow harmonics of order n, v_n scales with $v_2^{n/2}$, consistent with quark coalescence. However, the ratio v_4/v_2^2 is unexpectedly large. Some hadronic transport models are a factor of 2–3 lower than the data, but others achieve reasonable agreement. However, hydrodynamic model calculations provide the best predictions for v_2 compared with data. The characteristic collectivity feature—hadron mass dependence in the low p_t region—is observed. Hydrodynamic models seem to work for minimum bias data but not for centrality selected pion and antiproton data. The discrepancy for the central collision data may be because of nonflow effects and fluctuations in the data, and for the peripheral collisions from a failure of hydrodynamics. Perhaps, more work is needed to improve the hydrodynamic fits, especially for the different centrality bins, to make the case for early thermalization of collisions at RHIC. Awaiting further theoretical input or explanation are a number of STAR results, such as the large v_2 at high p_t [6] and the v_4 observations. v_4 is highly sensitive to initial conditions and the equation of state used in hydrodynamic calculations and therefore a challenge to all model descriptions. The data were systematized with fits to a blast-wave model. The blast-wave framework is capable of describing the large volume of experimental data up to p_t of 1 or 2 GeV/c using a relatively small set of fit parameters in each centrality interval, and the fit parameters are found to vary smoothly with centrality.

ACKNOWLEDGMENTS

We thank the RHIC Operations Group and RCF at BNL and NERSC at LBNL for their support. This work was supported in part by the HENP Divisions of the Office of Science of the U.S. DOE; the U.S. NSF; the BMBF of Germany; IN2P3, RA, RPL, and EMN of France; EPSRC of the United Kingdom; FAPESP of Brazil; the Russian Ministry of Science and Technology; the Ministry of Education and the NNSFC of China; Grant Agency of the Czech Republic, FOM and UU of the Netherlands, DAE, DST, and CSIR of the Government of India; Swiss NSF; and the Polish State Committee for Scientific Research.

APPENDIX A: BLAST-WAVE EQUATIONS

In both the surface shell and the filled elliptic cylinder cases the transverse-rapidity parametrization is extended to account for a possible fourth-harmonic anisotropy as follows:

$$\rho(\phi_b) = \rho_0 + \rho_2 \cos(2\phi_b) + \rho_4 \cos(4\phi_b), \tag{A1}$$

where the flow magnitude and anisotropy are accounted for by the ρ_n parameters and ϕ_b is the azimuthal angle of the boost source element defined with respect to the reaction plane, as shown in Fig. 37.

The distribution of source elements relative to ϕ_b in the case of a surface shell is written including second- and fourth-harmonic azimuthal anisotropy quantified by the s_2 and s_4 parameters respectively:

$$\Omega(\phi_b) = 1 + 2s_2 \cos(2\phi_b) + 2s_4 \cos(4\phi_b). \tag{A2}$$

When s_2 is positive more particles are boosted in plane than out of plane. In the case of a filled ellipse, the boost direction (ϕ_b) is assumed to be perpendicular to the freeze-out surface, which leads to a relationship between the space and boost azimuthal angles of the emitted particles as follows:

$$\tan(\phi_s) = (R_y/R_x)^2 \tan(\phi_b), \tag{A3}$$

with R_x and R_y the in plane and out-of-plane radii, respectively. For the v_n analysis $R = (R_x^2 + R_y^2)^{1/2}$ is an arbitrary radius, but when interferometry data are also fit, the units become significant. The system is bounded within an ellipse such as $\Omega(r, \phi_s) = \theta[\tilde{r}(\phi_s)]$ with θ the step function and

$$\tilde{r}(\phi_s) = \sqrt{[r\cos(\phi_s)/R_x]^2 + [r\sin(\phi_s)/R_y]^2}. \tag{A4}$$

In the filled ellipse case there is no explicit second- and fourth-harmonic parametrization of the spatial distribution of the particle emitting source because it is done implicitly by the ellipse parametrization. A profile, linear in transverse rapidity is used in the filled ellipse case as follows:

$$\rho(r, \phi_b) = [\rho_0 + \rho_2 \cos(2\phi_b) + \rho_4 \cos(4\phi_b)]\tilde{r}(\phi_b). \tag{A5}$$

The flow Fourier coefficients are defined by the following:

$$v_n = \langle \cos[n(\phi_p - \Psi)] \rangle, \tag{A6}$$

where ϕ_p is the azimuthal angle of the particle momentum. Assuming a Boltzmann plus flow distribution and longitudinal boost invariance, leads to the following expression for v_n:

$$v_n(p_t) = \frac{\int_{-\pi}^{\pi} d\phi_s \int_0^{\infty} r dr \int_0^{\pi} d\phi_p K_1[\beta(r,\phi_b)] \cos(n\phi_p) e^{\alpha(r,\phi_b)\cos(\phi_b-\phi_p)} \Omega(r,\phi_s)}{\int_{-\pi}^{\pi} d\phi_s \int_0^{\infty} r dr \int_0^{\pi} d\phi_p K_1[\beta(r,\phi_b)] e^{\alpha(r,\phi_b)\cos(\phi_b-\phi_p)} \Omega(r,\phi_s)}, \tag{A7}$$

with $\alpha(r,\phi_b) = (p_t/T)\sinh[\rho(r,\phi_b)]$ and $\beta_t(r,\phi_b) = (m_t/T)\cosh[\rho(r,\phi_b)]$. The relation between ϕ_b and ϕ_s is given by Eq. (A3). All the integrals are done numerically in the filled ellipse calculation to preserve the possibility of computing interferometry radii, even though the formula can be simplified to the following:

$$v_n(p_t) = \frac{\int_{-\pi}^{\pi} d\phi_b \int_0^{\infty} r dr K_1[\beta(r,\phi_b)] \cos(n\phi_b) I_n[\alpha(r,\phi_b)] \Omega(r,\phi_b)}{\int_{-\pi}^{\pi} d\phi_b \int_0^{\infty} r dr K_1[\beta(r,\phi_b)] I_0[\alpha(r,\phi_b)] \Omega(r,\phi_b)}. \tag{A8}$$

For the surface shell case the integral over r is trivial.

APPENDIX B: DERIVATION OF THE MIXED-HARMONIC EVENT-PLANE METHOD $v_1\{EP_1, EP_2\}$

Following the discussion in Ref. [23], we try to reduce the nonflow contribution of the first harmonic signal, v_1, by subtracting the contributions to the flow vector perpendicular to the reaction plane from the component within the reaction plane. As an estimate of the reaction plane we use the second-order event plane Ψ_2. Correlating the azimuthal angle of a particle, ϕ, with the first-order event plane, Ψ_1, one then obtains the following:

$$\begin{aligned}&\langle \cos(\phi - \Psi_2) \times \cos(\Psi_1 - \Psi_2) - \sin(\phi - \Psi_2) \times \sin(\Psi_1 - \Psi_2) \rangle \\ &\quad = \langle \cos(\phi + \Psi_1 - 2\Psi_2) \rangle \end{aligned} \tag{B1}$$

$$\begin{aligned}&= \langle \cos(\phi - \Psi_{\mathrm{RP}}) \times \cos(\Psi_1 - \Psi_{\mathrm{RP}}) \times \cos[2(\Psi_2 - \Psi_{\mathrm{RP}})] \rangle \\ &= \langle \cos(\phi - \Psi_{\mathrm{RP}}) \rangle \times \langle \cos(\Psi_1 - \Psi_{\mathrm{RP}}) \rangle \times \langle \cos[2(\Psi_2 - \Psi_{\mathrm{RP}})] \rangle \\ &\equiv v_1 \times \mathrm{Res}(\Psi_1) \times \mathrm{Res}(\Psi_2). \end{aligned} \tag{B2}$$

The factorization in left-hand side of Eq. (B2) is valid because of the statistical independence of the three factors. Although the resolution of the second-order event plane $\mathrm{Res}(\Psi_2)$ can be obtained by calculating the square root of the correlation of two subevent planes, the resolution of the first-order event plane $\mathrm{Res}(\Psi_1)$ can be calculated by considering the following:

$$\begin{aligned}&\langle \cos[2(\Psi_1 - \Psi_2)] \rangle \\ &\quad = \langle \cos^2(\Psi_1 - \Psi_{\mathrm{RP}}) \times \cos[2(\Psi_2 - \Psi_{\mathrm{RP}})] \rangle \\ &\quad = \langle \cos(\Psi_1 - \Psi_{\mathrm{RP}}) \rangle^2 \times \langle \cos[2(\Psi_2 - \Psi_{\mathrm{RP}})] \rangle \\ &\quad = \mathrm{Res}^2(\Psi_1) \times \mathrm{Res}(\Psi_2). \end{aligned} \tag{B3}$$

Combining the right-hand side of Eqs. (B2) and (B3) yields the following:

$$v_1\{\mathrm{EP}_1, \mathrm{EP}_2\} = \frac{\langle \cos(\phi + \Psi_1 - 2\Psi_2) \rangle}{\sqrt{\langle \cos[2(\Psi_1 - \Psi_2)] \rangle \times \mathrm{Res}(\Psi_2)}}.$$

This approach is similar to the three-particle correlation method of Borghini, Dinh, and Ollitrault [27]. One obtains their result by replacing the event plane angles Ψ_1 and Ψ_2 in the right-hand side of Eq. (B1) by emission angles of two particles [23].

Experimentally one wants to optimize the resolution of the second-order event plane by measuring it in a region c where the signal of v_2 is strong. This will be around midrapidity, preferentially. Conversely, the influence of nonflow can be reduced even further by measuring the azimuthal angle of the particle in one subevent, ϕ^a, and correlating it to the first-order event plane in the other subevent, Ψ_1^b. These subevents might by chosen randomly, or by dividing the acceptance into different regions in pseudorapidity. Because only half of all particles are used to determine each Ψ_1^a and Ψ_1^b, the statistical errors are increased by a factor of $\sqrt{2}$ compared to the three-particle cumulant method $v_1\{3\}$. The final observable looks like this:

$$v_1\{\mathrm{EP}_1, \mathrm{EP}_2\} = \frac{\left\langle \cos\left(\phi^a + \Psi_1^b - 2\Psi_2^c\right) \right\rangle}{\sqrt{\left\langle \cos\left(\Psi_1^a + \Psi_1^b - 2\Psi_2^c\right) \right\rangle \times \mathrm{Res}\left(\Psi_2^c\right)}}.$$

In our case each particle azimuth was correlated to the first-order event plane determined in the other subevent within the FTPCs, and to the second-order event plane measured in the TPC.

[1] W. Reisdorf and H. G. Ritter, Annu. Rev. Nucl. Part. Sci. **47**, 663 (1997).

[2] For an overview, see Proc. of Quark Matter 2004, J. Phys. G: Nucl. Part. Phys. **30**, (2004).

[3] RIKEN BNL Research Center Proceedings, vol. 62: *New Discoveries at RHIC—The Strongly Interacting Quark-Gluon Plasma*, BNL-72391-2004 (2004).

[4] M. Gyulassy and L. McLerran, Nucl. Phys. **A750**, 30 (2005).

[5] C. Adler *et al.* (STAR Collaboration), Phys. Rev. Lett. **90**, 032301 (2003).

[6] J. Adams *et al.* (STAR Collaboration), Phys. Rev. Lett. **93**, 252301 (2004).

[7] M. Anderson *et al.*, Nucl. Instrum. Methods A **499**, 659 (2003).

[8] K. H. Ackermann *et al.*, Nucl. Instrum. Methods A **499**, 713 (2003).

[9] A. Braem *et al.*, Nucl. Instrum. Methods A **499**, 720 (2003); B. Lasiuk *et al.*, Nucl. Phys. **A698**, 452c (2002).

[10] C. Adler *et al.* (STAR Collaboration), Phys. Rev. Lett. **89**, 202301 (2002).

[11] Mike Miller, Ph.D. dissertation, Yale University (2003).

[12] C. Adler *et al.* (STAR Collaboration), Phys. Rev. Lett. **87**, 182301 (2001).

[13] Aihong Tang, Ph.D. dissertation, Kent State University (2002), http://phys.kent.edu/PhDdiss/.

[14] W. S. Deng, Ph.D. dissertation, Kent State University (2002); B. E. Norman, Ph.D. dissertation, Kent State University (2003), http://phys.kent.edu/PhDdiss/.

[15] C. Adler *et al*. (STAR Collaboration), Phys. Rev. Lett. **89**, 132301 (2002).

[16] J. Adams *et al*. (STAR Collaboration), Phys. Rev. Lett. **92**, 182301 (2004).

[17] J. Castillo (STAR Collaboration), J. Phys. G: Nucl. Part. Phys. **30**, S1207 (2004).

[18] A. M. Poskanzer and S. A. Voloshin, Phys. Rev. C **58**, 1671 (1998).

[19] K. H. Ackermann *et al*. (STAR Collaboration), Phys. Rev. Lett. **86**, 402 (2001).

[20] J. Adams *et al*. (STAR Collaboration), Phys. Rev. Lett. **92**, 052302 (2004).

[21] N. Borghini, P. M. Dinh, and J.-Y. Ollitrault, Phys. Rev. C **64**, 054901 (2001).

[22] C. Adler *et al*. (STAR Collaboration), Phys. Rev. C **66**, 034904 (2002).

[23] J. Adams *et al*. (STAR Collaboration), Phys. Rev. Lett. **92**, 062301 (2004).

[24] A. H. Tang (STAR Collaboration), J. Phys. G: Nucl. Part. Phys. **30**, S1235 (2004), arXiv: nucl-ex/0403018.

[25] M. D. Oldenburg (STAR Collaboration), arXiv: nucl-ex/0403007.

[26] A. M. Poskanzer (STAR Collaboration), J. Phys. G: Nucl. Part. Phys. **30**, S1225 (2004), arXiv: nucl-ex/0403019.

[27] N. Borghini, P. M. Dinh, and J.-Y. Ollitrault, Phys. Rev. C **66**, 014905 (2002).

[28] N. Borghini, P. M. Dinh, and J.-Y. Ollitrault, *Proceedings of the International Workshop on the Physics of the Quark-Gluon Plasma*, Palaiseau, France, 4–7 September 2001, arXiv: nucl-ex/0110016.

[29] M. Belt Tonjes (PHOBOS Collaboration), J. Phys. G: Nucl. Part. Phys. **30**, S1243 (2004); arXiv: nucl-ex/0403025; S. Manly, arXiv: nucl-ex/0405029; B. B. Back, arXiv: nucl-ex/0407012 (submitted to Phys. Rev. C Rapid Comm.); C. M. Vale, arXiv: nucl-ex/0410008.

[30] D. Molnar and S. A. Voloshin, Phys. Rev. Lett. **91**, 092301 (2003); R. C. Hwa and C. B. Yang, Phys. Rev. C **67**, 064902 (2003); R. J. Fries, B. Müller, C. Nonaka, and S. A. Bass, *ibid.* **68**, 044902 (2003); V. Greco, C. M. Ko, and P. Levai, *ibid.* **68**, 034904 (2003); V. Greco, C. M. Ko, and P. Levai, Phys. Rev. Lett. **90**, 202302 (2003); R. J. Fries, B. Müller, C. Nonaka, and S. A. Bass, *ibid.* **90**, 202303 (2003); R. C. Hwa and C. B. Yang, Phys. Rev. C **70**, 024905 (2004); **70**, 024904 (2004); D. Molnar, arXiv: nucl-th/0408044; S. Pratt and S. Pal, arXiv: nucl-th/0409038.

[31] P. Huovinen, P. F. Kolb, U. W. Heinz, P. V. Ruuskanen, and S. A. Voloshin, Phys. Lett. **B503**, 58 (2001).

[32] S. S. Adler *et al*. (PHENIX Collaboration), Phys. Rev. Lett. **91**, 182301 (2003).

[33] J. Adams *et al*. (STAR Collaboration), Phys. Rev. Lett. **91**, 072304 (2003); S. S. Adler *et al*. (PHENIX Collaboration), *ibid.* **91**, 072303 (2003); B. B. Back *et al*. (PHOBOS Collaboration), *ibid*. **91**, 072302 (2003); I. Arsene *et al*. (BRAHMS Collaboration), *ibid*. **91**, 072305 (2003).

[34] R. C. Hwa and C. B. Yang, Phys. Rev. Lett. **93**, 082302 (2004).

[35] B. B. Back *et al*. (PHOBOS Collaboration), Phys. Rev. Lett. **89**, 222301 (2002).

[36] M. Gyulassy and M. Plümer, Phys. Lett. **B243**, 432 (1990); X. N. Wang and M. Gyulassy, Phys. Rev. Lett. **68**, 1480 (1992); R. Baier, D. Schiff, and B. G. Zakharov, Annu. Rev. Nucl. Part. Sci. **50**, 37 (2000).

[37] J. Adams *et al*. (STAR Collaboration), Phys. Rev. Lett. **91**, 172302 (2003); Phys. Rev. Lett. **91**, 072304 (2003).

[38] C. Adler *et al*. (STAR Collaboration), Phys. Rev. Lett. **90**, 082302 (2003).

[39] M. Miller and R. Snellings, arXiv: nucl-ex/0312008.

[40] P. F. Kolb, Phys. Rev. C **68**, 031902(R) (2003), and private communication.

[41] S. A. Voloshin and Y. Zhang, Z. Phys. C **70**, 665 (1996).

[42] J.-Y. Ollitrault, Nucl. Phys. **A590**, 561c (1995).

[43] H. Sorge, Phys. Lett. **B402**, 251 (1997).

[44] H. Sorge, Phys. Rev. Lett. **82**, 2048 (1999).

[45] J.-Y. Ollitrault, Phys. Rev. D **46**, 229 (1992).

[46] D. Teaney, J. Lauret, and E. V. Shuryak, Phys. Rev. Lett. **86**, 4783 (2001).

[47] S. S. Adler *et al*. (PHENIX Collaboration), Phys. Rev. Lett. **91**, 172301 (2003).

[48] V. Greco and C. M. Ko, Phys. Rev. C **70**, 024901 (2004); X. Dong, S. Esumi, P. Sorensen, N. Xu, and Z. Xu, Phys. Lett. **B597**, 328 (2004).

[49] P. F. Kolb, L.-W. Chen, V. Greco, and C. M. Ko, Phys. Rev. C **69**, 051901(R) (2004).

[50] L.-W. Chen, C. M. Ko, and Z.-W. Lin, Phys. Rev. C **69**, 031901(R) (2004).

[51] M. Bleicher and H. Stöcker, Phys. Lett. **B526**, 309 (2002).

[52] Z.-W. Lin and C. M. Ko, Phys. Rev. C **65**, 034904 (2002); L.-W. Chen and C. M. Ko, arXiv: nucl-th/0409058; Z.-W. Lin, C. M. Ko, B.-A. Li, B. Zhang, and S. Pal, arXiv: nucl-th/0411110.

[53] B. Zhang, M. Gyulassy, and C. M. Ko, Phys. Lett. **B455**, 45 (1999).

[54] L.-W. Chen, V. Greco, C. M. Ko, and P. F. Kolb, Phys. Lett. **B605**, 95 (2005).

[55] D. Teaney, J. Lauret, and E. V. Shuryak, Nucl. Phys. **A698**, 479 (2002).

[56] E. Zabrodin, L. Bravina, C. Fuchs, and A. Faessler, Prog. Part. Nucl. Phys. **53**, 183 (2004); G. Burau *et al*., arXiv: nucl-th/0411117.

[57] P. F. Kolb and U. Heinz, in "Quark Gluon Plasma 3," edited by R. C. Hwa and X. N. Wang (World Scientific, Singapore), arXiv: nucl-th/0305084.

[58] P. F. Kolb, arXiv: nucl-th/0407066.

[59] U. Heinz, arXiv: nucl-th/0407067.

[60] P. Huovinen, private communication (2004). $T_c = 165\,\text{MeV}$, $T_f = 130\,\text{MeV}$, EoS = Q.

[61] P. F. Kolb and R. Rapp, Phys. Rev. C **67**, 044903 (2003).

[62] C. Adler *et al*. (STAR Collaboration), Phys. Rev. Lett. **87**, 082301 (2001); K. Adcox *et al*. (PHENIX Collaboration), *ibid*. **88**, 192302 (2002).

[63] T. Hirano, Phys. Rev. C **65**, 011901(R) (2002).

[64] U. Heinz and P. F. Kolb, J. Phys. G: Nucl. and Part. Phys. **30**, S1229 (2004).

[65] C. Alt *et al*. (NA49 Collaboration), Phys. Rev. C **68**, 034903 (2003).

[66] E. Schnedermann, J. Sollfrank, and U. Heinz, Phys. Rev. C **48**, 2462 (1993).

[67] M. Csanád, T. Csörgő, B. Lörstad, and A. Ster, J. Phys. G: Nucl. Part. Phys. **30**, S1079 (2004).

[68] F. Retiere and M. A. Lisa, Phys. Rev. C **70**, 044907 (2004).

[69] B. Tomášik, arXiv: nucl-th/0409074.

[70] J. Adams *et al*. (STAR Collaboration), Phys. Rev. Lett. **92**, 112301 (2004).